Molecular Cancer

RESEARCH

Open Access

GP73-dependent regulation of exosome biogenesis promotes colorectal cancer liver metastasis

Linfei Huang[1†], Meng Wei[2,3†], Huilong Li[1†], Mingxin Yu[4†], Luming Wan[1†], Ruzhou Zhao[1†], Qi Gao[5], Lijuan Sun[5], Xufeng Hou[5], Yunhai Mo[2,3], Qing Huang[2,3], Lan Zhen[2,3], Xiaopan Yang[1], Jingfei Li[1], Nan Wang[6], Chundong Zhang[7], Haoran Jin[8], Li Zhou[1], Yixin Xu[2,3], Haotian Lin[1], Xuhui Zhang[5], Boan Li[9*], Yue Han[10*], Jing Yuan[11*], Rui Zhang[8*], Feixiang Wu[2,3*], Hui Zhong[5*] and Congwen Wei[1*]

Abstract

Colorectal cancer (CRC) liver metastasis is the main cause of cancer-related mortality. How liver influences intercellular communication to support CRC liver metastasis remains unknown. Herein, we link GP73, whose chronic upregulation in hepatocytes triggers non-obese metabolic-dysfunction associated steatotic liver disease (MASLD) in mice, with exosome biogenesis and CRC liver metastasis. Mice with high liver GP73 expression exhibited increased CRC liver metastasis in an exosome-dependent manner. GP73 modulated the cholesterol contents in endosomal compartments to promote exosome production. Quantitative proteomics revealed GP73 reshaped hepatocyte exosomal proteome and produced NAV2-rich exosomes. Clinically, serum GP73 levels positively correlated with exosomal NAV2 levels in CRC patients with liver metastasis. Knockdown of liver NAV2 suppressed enhanced CRC liver metastasis in GP73-induced non-obese mice, and GP73 blockade mitigated the increased CRC liver metastasis in obese mice fed by high-fat diet or high-fructose diet. Our findings suggest GP73 blockade as a potential therapeutic strategy for mitigating CRC liver metastasis.

†L. Huang, M. Wei, H. Li, M. Yu, L. Wan and R. Zhao contributed equally to this work.

*Correspondence:
Boan Li
lba@263.net
Yue Han
doctorhan@163.com
Jing Yuan
yuanjing6216@163.com
Rui Zhang
zhangrui@cancerhosp-ln-cmu.com
Feixiang Wu
wufx2013@163.com
Hui Zhong
hui.zhong@youngenbiomed.com.cn
Congwen Wei
weicongwen@aliyun.com

Full list of author information is available at the end of the article

Significance

GP73 closely correlated with exosome biogenesis and CRC liver metastasis, and GP73 blockade may merit exploration as a potential therapeutic strategy for mitigating CRC liver metastasis.

Keywords Golgi protein 73, Exosome, Colorectal cancer, Metastasis

Introduction

Colorectal cancer (CRC) is the third most common malignancy and the second leading cause of cancer-related death worldwide [1–3]. CRC progresses through an adenoma-to-carcinoma sequence, and approximately 70% of CRC patients develop metastasis preferentially to the liver (CRLM) [4–7]. CRC patients with inoperable liver metastasis respond poorly to most forms of combination therapy, and liver metastasis in these patients is the major cause of death [5, 8–10]. Throughout the course of tumor development, tumor cell hierarchies and the liver metabolic status play important roles in cancer liver metastasis [11, 12]. Obesity and MASLD are associated with an increased incidence of CRC liver metastasis and worsening prognosis [13, 14]. Experimental evidence indicates that obese adipocytes and steatotic hepatocytes promote liver metastasis by inflammatory factors, fatty acid transfer, direct interaction with the tumor, or exosome transfer [14–16]. Non-obese MASLD constitutes over 40% of MASLD cases [17], and patients with non-obese MASLD have a two times higher liver-related mortality rate than that in the obese MASLD population [18, 19]. GP73 is highly expressed in various liver diseases, particularly in the livers of patients with non-obese and obese MAFLD. However, there are currently no studies investigating the association between elevated GP73 expression and the occurrence of colorectal cancer liver metastasis. Therefore, identifying the central axis that leads to CRC metastasis in non-obese and obese individuals with MASLD is thus critical for designing medicines that can halt tumor liver metastasis.

Exosomes, nanovesicles with a lipid bilayer membrane, are vesicles generated from intraluminal vesicles (ILVs) of multivesicular bodies (MVBs), which are membrane-bound compartments linked to endosomal system [20, 21]. Organization of membrane subdomains through the lipid composition of MVB membranes modulates exosome biogenesis [22, 23]. Cancer cells secrete larger amounts of exosomes than healthy cells, as higher numbers of exosomes have been detected in the plasma of cancer patients as well as in tumor cell cultures [24, 25]. Exosomal cargo is composed of proteins, lipids, and nucleic acids [26]. Recently, tumor-derived exosomes have been increasingly recognized as contributors to tumor progression, invasion, and metastasis via horizontal transfer of regulatory molecules to target cells, and they can mediate tumor-stroma communication and pre-metastatic niche formation [14, 27, 28].

Golgi protein 73 (GP73, also referred to as Golph 2 and GOLM1) is a 73 kDa transmembrane glycoprotein localized in cis-Golgi complex [29]. GP73 functions as a critical factor in modulating cancer metastasis by regulating the trafficking of epithelial-mesenchymal transition (EMT)-associated factors [30]. It is expressed primarily in epithelial cells and upregulated in hepatocytes of patients with liver diseases [31], multiple cancers [32], MASLD [33], or diabetes [34, 35]. Chronic upregulation of GP73 in hepatocytes contributes to early onset of non-obese MASLD in mice [33]. Our study suggests that GP73 overlapped with MVBs and stimulated exosome biogenesis depending on its cholesterol-binding ability. Notably, GP73 reshaped hepatocyte exosomal proteome, and NAV2 was implicated in the mechanism by which GP73 promoted CRC liver metastasis. Targeting GP73 effectively suppressed CRC liver metastasis in mice with GP73-induced non-obese MASLD and diet induced-obese MASLD.

Results

Liver GP73 expression is pathologically elevated in CRC patients with liver metastasis

Elevated serum GP73 levels have been observed in hepatocellular carcinoma (HCC) and are associated with poor prognosis in human patients with HCC [36, 37]. However, clinical relevance of GP73 expression in patients with liver-metastatic cancer remains largely unknown. We examined plasma GP73 expression in 50 healthy controls, 53 CRC patients without liver metastasis (CRNLM), and 34 CRLM (CRC patients with liver metastasis) (Supplemental Table 1). Compared with healthy controls, patients with CRC had higher GP73 levels. In particular, GP73 expression was induced to the highest level in CRLM (Fig. 1A). To continue the investigation, we analyzed GP73 expression in liver tissues from 4 healthy subjects (normal liver tissue, NLT) and 8 CRLM using immunofluorescence microscopy and RT-qPCR (Supplemental Table 2). As previously reported, a minority of hepatocytes in NLT exhibited GP73 immunoreactivity with low staining intensity [31]. In contrast, GP73 immunoreactivity was seen in all CRLM (8/8), with robust staining intensity and primarily co-localized with albumin in hepatocytes (Fig. 1B-C; Supplementary Fig. S1A-B). GP73 mRNA expression was upregulated in 6 of the 8 CRLM liver tissues (Supplementary Fig. S1C).

Together, our data strongly suggests a close association between the upregulated GP73 protein levels in the patient livers and the occurrence of CRC liver metastasis.

High GP73 expression in the liver increases CRC liver metastasis mainly in an exosome-dependent manner

We next sought to determine whether hepatocytes with high GP73 expression can influence CRC liver metastasis. To this end, we first generated mice with high liver GP73 expression by tail vein injection of AAV-V or AAV-GP73. MC38 cells were then injected intrasplenically 28 days after AAV injection to allow AAV-GP73 expression in the livers (Supplementary Fig. S1D-F). Interestingly, GP73 expression was higher in hepatocytes at the margins of metastatic tumors (Supplementary Fig. S1G). Notably, the overall area, number, and ratio of liver metastatic foci were significantly increased in AAV-GP73-treated mice (Fig. 1D-E; Supplementary Fig. S1H-I). Strikingly, the metastasis tumor growth was partially blocked in AAV-GP73-treated mice after injection of GW4869 (1.25 mg/kg/day administered continuously for 14 days) to inhibit exosome production (Fig. 1F-G; Supplementary Fig. S1J-L). We also investigated the effects of GW4869 on hepatocyte viability in vitro. AML-12 cells were treated with GW4869 at concentrations ranging from 0.5 to 40 μM, and no apparent impact on hepatocyte viability was observed (Supplementary Fig. S1M). Therefore, upregulated GP73 in the liver enhances CRC cancer liver metastasis mainly in an exosome-dependent manner.

GP73 promotes exosome production

We then attempted to elucidate the role of GP73 in exosome biogenesis. To this end, exosomes from the conditioned media of Huh-7 hepatocytes transfected with Flag-vector (ExoCtr) or Flag-GP73 (ExoGP73) were purified by differential ultracentrifugation (Supplementary Fig. S2A-B). The abundance of ALIX, TSG101, and CD63 was increased along with the GP73 overexpression in host cells (Supplementary Fig. S2B). ExoCtr and ExoGP73 displayed similar morphology, size distributions, and molecular compositions, as shown by transmission electron microscopy (TEM), nanoparticle tracking analysis (NTA), and immunoblotting (Fig. 2A-C). Dulbecco's phosphate-buffered saline (DPBS) and standard nanoparticles were employed as negative and positive controls, respectively (Supplementary Fig. S2C). The electron micrographs revealed that the cup-shaped, rounded exosomes exhibited no visual evidence of contamination by membrane fragments (Fig. 2A). ExoCtr and ExoGP73 contained similar amounts of the exosomal markers CD63 and TSG101 when loaded with the same amount of exosomal particles (Fig. 2C). Strikingly, more exosome particles were detected in the culture media from Flag-GP73-transfected Huh-7 cells (Fig. 2D) and GP73 also increased exosome protein levels (Fig. 2F). GP73 also increased exosome particles and exosome proteins released from normal hepatocyte AML-12 cells (Fig. 2E, G).

To further study the role of GP73 in exosome secretion in a more physiological context, mice with global GP73 knockout (GP73-KO) were generated (Supplementary Fig. S2D), and the GP73 levels in the serum from GP73-KO and wild-type (WT) mice were quantified (Supplementary Fig. S2E). The genotype had no effect on the average vesicular diameter (Fig. 2H; Supplementary Fig. S2F). Intriguingly, the concentration of exosome particles in the same amount of serum was 70% lower in GP73-KO mice than in WT mice (Fig. 2I). Consistent with this finding, serum from AAV-GP73-injected mice contained more exosome particles than serum from AAV-V-injected mice, with no noted difference in vesicular size (Fig. 2J-L; Supplementary Fig. S2G). Together, these data strongly support the role of GP73 in the regulation of exosome biogenesis both in vitro and in vivo.

GP73 overlaps with endosomal compartments and increases the MVB number

Exosome biogenesis consists of three processes: the formation of ILVs, the generation of MVBs, and secretion of exosomes upon fusion of these compartments with the plasma membrane (PM) [38]. The effect of GP73 on exosome biogenesis prompted us to investigate whether it is localized with endosomal compartments upon overexpression. To this end, we assessed the co-localization of GP73 with a marker of early endosomes (Rab5), a marker of recycling endosomes (Rab11), and a marker of late endosomes (Rab7) by immunofluorescence staining [39]. In GP73-overexpressing cells, GP73 was localized in early, recycling, and late endosomes throughout the endocytosis pathway (Fig. 3A-B). By live-cell imaging, we found that GP73 puncta exhibited active movement and were constitutively overlapped in CD63-positive MVBs and their sites of fusion with the PM (Fig. 3C-E). In addition, both proteins were detected in some larger internal compartments (Fig. 3C). Using hepatocyte growth factor-regulated tyrosine kinase substrate (HRS) staining as an MVB marker, we found that GP73 overexpression led to an increased MVB number per cell, whereas GP73 knockdown significantly reduced the MVB number (Fig. 3F-H; Supplementary Fig. S3A-B). Collectively, these data support the idea that GP73 mainly affects the MVB pathway.

GP73 binds cholesterol and modulates the cholesterol contents in endosomal compartments

We then sought to understand the mechanisms underlying the role of GP73 in regulating MVB numbers and hence exosome production. Based on the gene

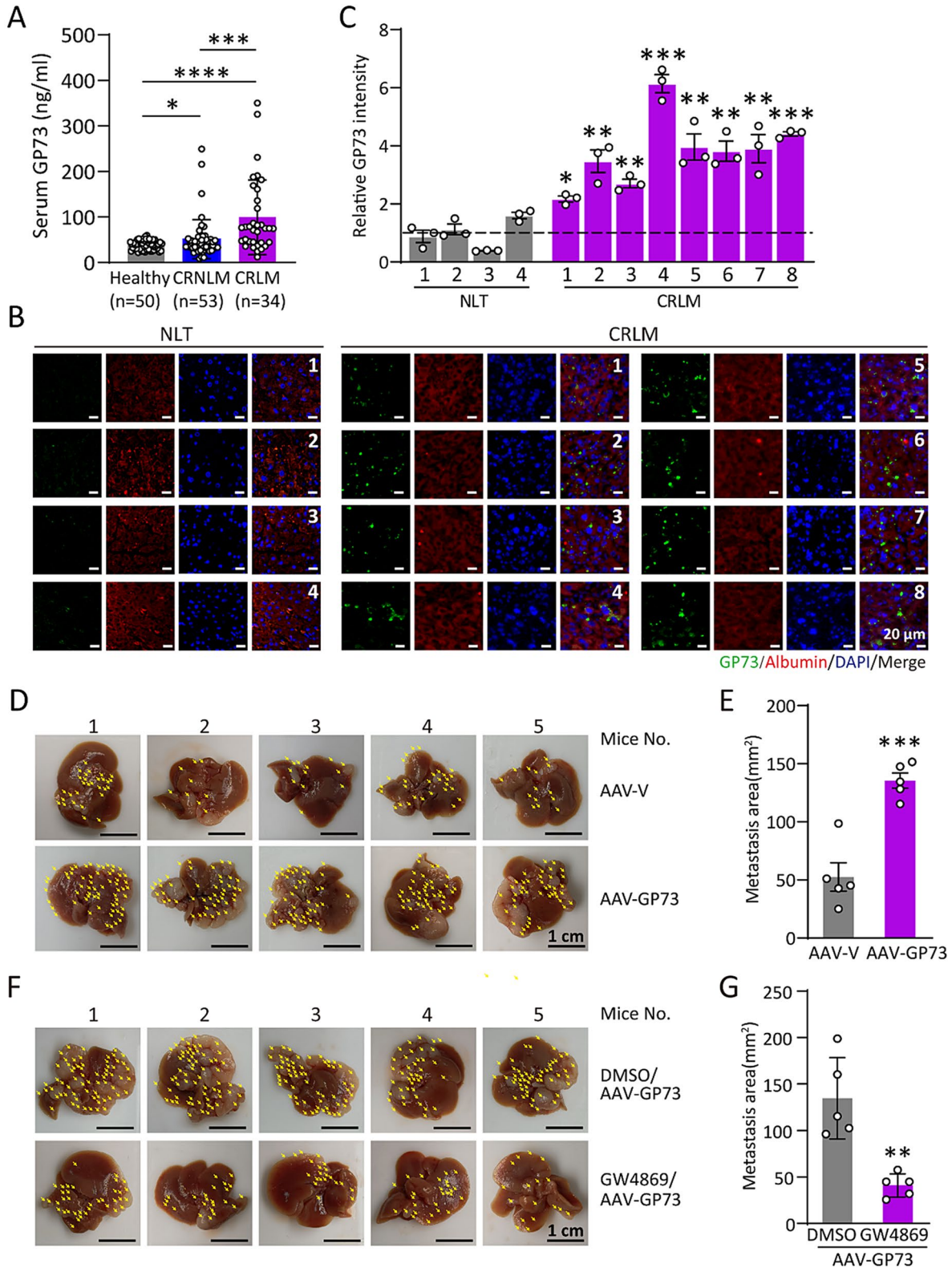

Fig. 1 (See legend on next page.)

(See figure on previous page.)

Fig. 1 Liver GP73 expression is pathologically elevated in CRC patients with liver metastasis. (**A**) Serum GP73 levels in healthy controls (Healthy, $n = 50$), CRC patients without liver metastasis (CRNLM, $n = 53$), and CRC patients with liver metastasis (CRLM, $n = 34$). (**B**) Representative immunofluorescence images of GP73 and Albumin staining in livers from healthy controls (normal liver tissue, NLT, $n = 4$) and CRLM ($n = 8$). Green, GP73 staining; red, Albumin staining; blue, nuclear DAPI staining; scale bars, 20 μm. (**C**) Relative GP73 staining intensity in samples from (**B**); the average GP73 intensity of healthy controls was set to 1. (**D**-**E**) Representative images of metastatic liver from AAV-V- or AAV-GP73-injected mice inoculated with MC38 cells via intrasplenic injection (**D**, $n = 5$) and quantification of metastatic tumor size (**E**). (**F**-**G**) Representative images of metastatic liver from AAV-GP73-injected mice inoculated with MC38 cells via intrasplenic injection in the presence of GW4869 (**F**, $n = 5$) and quantification of metastatic tumor size (**G**). The arrows show liver metastastic foci. All images were representative of at least three biological replicates. All quantitative data were presented as the mean ± SD. Statistical significance was determined using one-way ANOVA with the Bonferroni correction (**A**, **C**) or two-tailed Student's t test (**E**, **G**)

expression microarray data (Gene Expression Omnibus database, GSE163918) of AAV-V and AAV-GP73 mice livers reported by Peng's group [33], high GP73 protein levels in mice livers were closely related with apparently increased expression levels of genes involved in the cholesterol biosynthesis, binding, and transport pathways (Supplementary Fig. S4A). Alterations in cholesterol levels can influence intracellular transport mechanisms, including the formation and maturation of endosomes and MVB, which are crucial precursors to exosome generation. A search for cholesterol-regulated motifs in the primary sequence of GP73 identified a putative conserved cholesterol recognition amino acid consensus (CRAC) motif: (L/V)-X_{1-5}-(Y)-X_{1-5}-(K/R) [40] (Fig. 4A). Moreover, the CRAC motif is immediately preceded by a similar but inverted cholesterol-recognition motif called a CARC motif (Fig. 4A). To test the ability of GP73 to bind lipids, we expressed and purified the GFP-tagged full-length GP73 protein. Using a fluorescent cholesterol binding assay, we found that GP73-GFP interacted with cholesterol with an EC_{50} of 12.6 ± 4.6 nM (Fig. 4B; Supplementary Fig. S4B). The specificity of GP73 for cholesterol was examined by its capacity to bind the structurally distinct sterols 25-hydroxycholesterol (25-HC), 27-hydroxycholesterol (27-HC), campesterol, and epicholesterol (Supplementary Fig. S4C). Notably, GP73 had equivalent affinities for cholesterol and other four sterols we tested (Fig. 4B; Supplementary Fig. S4B).

In contrast, deletion of the CRAC domain (ΔCRAC) or double mutation of the CARC Phe90 and CRAC Tyr99 residues double mutant (DM) in mouse GP73 (F90I-Y99I) reduced the cholesterol-induced change in fluorescence (Fig. 4C). To further delineate the specific role of the CARC-CRAC domain of GP73, we carried out in vitro binding assays using a peptide that encompasses both motifs (amino acid residues 83–105; Supplementary Fig. S4D). Titrating the peptide with increasing concentrations of cholesterol yielded a dose dependent, saturable increase in the 350 nm fluorescence emission of a Tryptophan residue within the peptide, suggesting a conformational change induced by cholesterol (Fig. 4D). Mutating the obligate Tyr99 residue in the CRAC motif to Ile reduced the cholesterol-induced change in fluorescence, whereas DM abolished the cholesterol-induced change in fluorescence altogether (Fig. 4D). Although potential confounds, like buffer pH value, ion strength, and peptide aggregation etc., may affect the Tryptophan emission fluorescence during the synthetic peptides-cholesterol binding, consistent results were obtained from the assays mentioned above that Phe90 and Tyr99 are vital residues for GP73-cholesterol binding (Fig. 4C-D).

The active movement of GP73 between different compartments and its ability to bind cholesterol with high affinity suggest that GP73 might contribute to the regulation of cholesterol flux in endosomal compartments. Notably, GP73 overexpression led to substantial increases in the MVB area and filipin intensity in the MVB compartment (Fig. 4E-H). In contrast, the GP73-DM, which failed to bind cholesterol and promote cholesterol accumulation in the MVB compartment, also lost the ability to increase CD63 positive MVB numbers (Fig. 4E-J) and the relevant exosome yields were notably decreased (Supplementary Fig. S4E-F). These results suggest that GP73 regulates exosome biogenesis by modulating the cholesterol contents through an interaction with cholesterol.

Exosomes derived from GP73-high hepatocytes promote metastasis

We then tested whether the changes in exosome secretion could alter the migratory ability of the recipient cancer cells (Fig. 5A). Exosomes can migrate across the membrane separating the upper and lower compartments. Forty-eight hours later, the MC38 cells exhibited increased migration and invasion capabilities when co-cultured with Flag-GP73-tranfected cells (Fig. 5A-D; Supplementary Fig. S5A). Notably, MC38 cells exhibited relatively slower migration when cultured with DM-transfected cells (Fig. 5B, C). To further determine whether exosomes from GP73-high hepatocytes directly play a role in liver metastasis, we prepared liver exosomes from AAV-V-injected mice (ExoCtr)- or AAV-GP73-injected mice (ExoGP73) (Supplementary Fig. S5B). The physicochemical characteristics of these in vivo liver exosomes are similar to those of typical exosomes isolated from in vitro cell conditioned medium (Fig. 5E-F; Supplementary Fig. S5C). Internalization of ExoCtr and ExoGP73 exosomes was quantified by PKH26 labeling and fluorescent microscopy. Almost all the MC38 cell nuclei were surrounded by red fluorescent spots which indicated that PKH26-labeled ExoCtr and ExoGP73 were

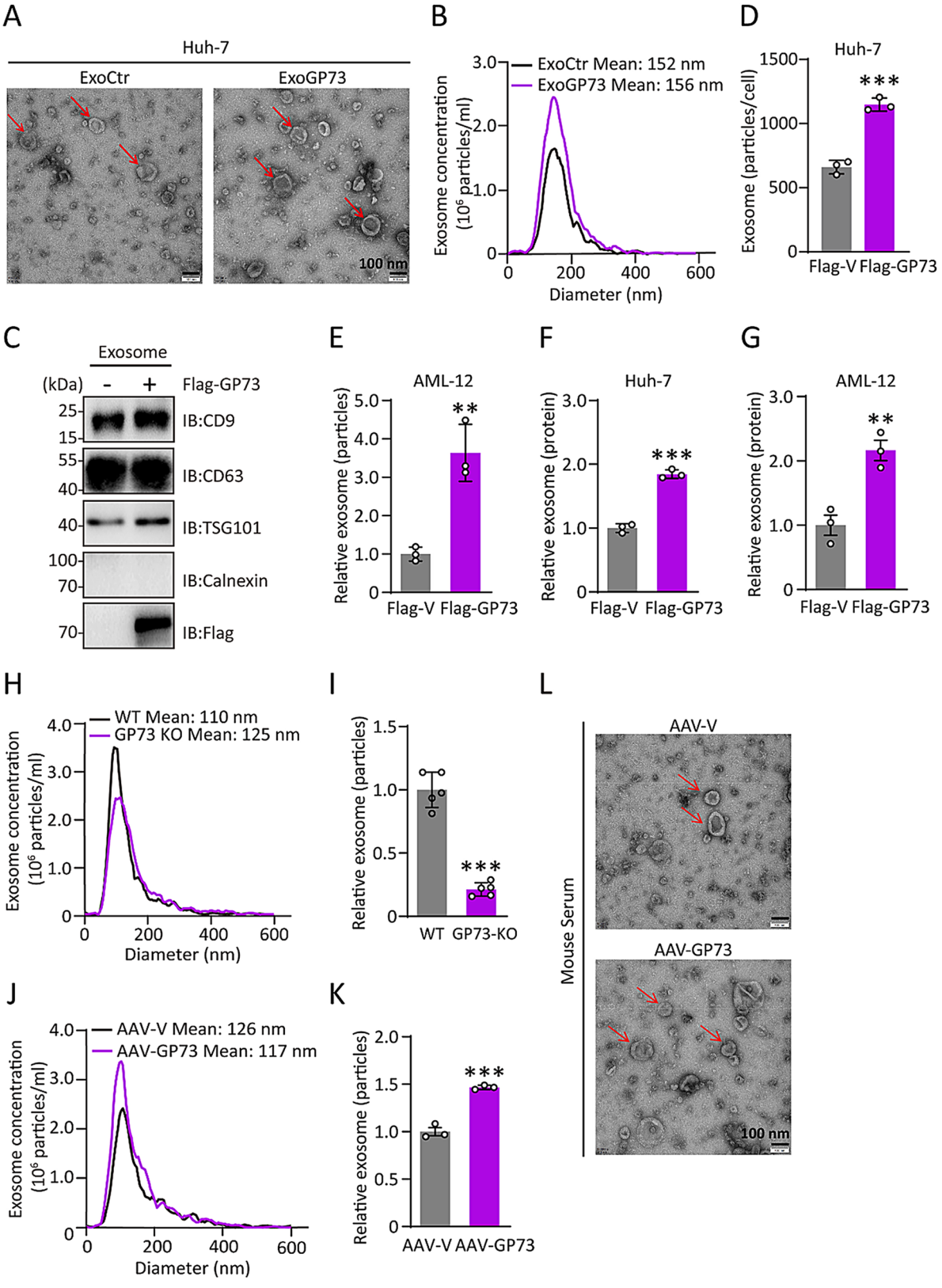

Fig. 2 (See legend on next page.)

(See figure on previous page.)

Fig. 2 GP73 promotes exosome production. (**A**) Transmission electron microscopy of purified exosomes derived from Huh-7 cells transfected with Flag-vector (ExoCtr) or Flag-GP73 (ExoGP73). (**B**) Representative NTA of ExoCtr and ExoGP73. The x-axis shows the diameter of the vesicles, and the y-axis shows the concentration (10^6 particles/mL) of the vesicles. (**C**) Immunoblotting of exosome markers (CD9, CD63, and TSG101) and negative marker of exosomes (Calnexin) in the purified Huh-7 cell-derived ExoCtr and ExoGP73. Molecular weights (in kDa) are shown to the left. (**D**-**E**) Exosome particles released from equal numbers of Flag-V or Flag-GP73-transfected Huh-7 cells (**D**) and AML-12 cells (**E**). The abundances of particles in exosomes released from Flag-V transfected cells were normalized to 1 ($n = 3$). (**F**-**G**) Exosomal protein released from equal numbers of Flag-V- or Flag-GP73-transfected Huh-7 cells (**F**) and AML-12 cells (**G**). The abundances of proteins in exosomes released from Flag-V transfected cells were normalized to 1 ($n = 3$). (**H**-**K**) Representative NTA of purified serum exosomes and exosome particles isolated from 0.5 mL of serum derived from WT and GP73-KO mice (**H**, **I**) ($n = 5$), and from AAV-V- or AAV-GP73-injected mice (**J**, **K**) ($n = 3$). (**L**) Transmission electron microscopy of purified serum exosomes from AAV-V- or AAV-GP73-injected mice. Cell-based studies were performed independently at least three times with comparable results. All quantitative data were presented as the mean ± SD. All images were representative of at least three biological replicates. Statistical significance was determined using two-tailed Student's t test (**D**, **E**, **F**, **G**, **I**, **K**)

uptaken by MC38 cells and there was no significant difference between ExoCtr and ExoGP73 uptake efficiency (Supplementary Fig. S5D). Notably, MC38 cells treated with ExoGP73 directly exhibited an enhanced ability to migrate compared with ExoCtr-treated MC38 cells in wound healing migration assays (Fig. 5G). The results of transwell assays suggested that ExoGP73 significantly enhanced cell motility and invasion (Fig. 5H-I). EMT-related markers were also examined, and it was found that when co-cultured with Flag-GP73-transfected cells, there was a decreased expression of E-cadherin, and an increased expression of N-cadherin, SERPINE1, Vimentin, Snai1, and TWIST1 (Supplementary Fig. S5E). To further determine whether ExoGP73 directly play a role in liver metastasis in vivo, ExoGP73 or ExoCtr was administered to WT mice via tail vein injection twice a week for three weeks, a process that we previously defined as "education" and was initiated one week before intrasplenic injection of MC38 cells (Fig. 5J; Supplementary Fig. S5F). Five of five mice treated with ExoGP73 had severe liver metastasis (Fig. 5K-L). ExoGP73 also increased the size and number of metastatic foci (Fig. 5M-N). Therefore, ExoGP73 enhances metastatic tumor growth in the livers.

GP73 mediates the production of NAV2-rich exosomes

To identify the factor possibly involved in the prometastatic effect of ExoGP73, we next conducted quantitative proteomic profiling of ExoCtr and ExoGP73 using TMT-labeled mass spectrometry (MS). With a threshold of $|Zq| > 1.5$, 59 proteins were more abundant and 5 were less abundant in ExoGP73 than in ExoCtr (Fig. 6A). Interestingly, GP73 was also enriched in ExoGP73, indicating that intracellular GP73 was also packaged into exosomes (Fig. 6A). Among the 59 upregulated proteins enriched in ExoGP73, 17 (26.6%) were categorized as endoplasmic reticulum (ER) proteins (Fig. 6B). Therefore, GP73 promoted the sorting of ER protein components into exosomes. Gene Ontology (GO) enrichment analysis showed that the most significantly enriched biological processes related to ExoGP73 were the glycoprotein biosynthetic process, glycoprotein metabolic process, and response to ER stress (Fig. 6C). KEGG analysis indicated that proteins involved in multiple pathways, including protein export, protein processing in the ER, and N-glycan biosynthesis, were enriched in ExoGP73 (Fig. 6D). Additional differentially expressed proteins in ExoGP73 included MGST1 [41] and MGST2 [42], which are usually associated with HCC, were more abundant in ExoGP73 than in ExoCtr (Fig. 6A).

One specific top-ranked differentially expressed protein, NAV2, attracted our attention due to its important roles in development, stem cell niche formation, and aggressive tumor metastasis [43] (Fig. 6A). To confirm the proteomics results, we conducted immunoblot analysis with an NAV2 antibody and found that NAV2 was almost undetectable in exosomes isolated from the supernatants of Huh-7 cells transfected with the vector control. However, under GP73 overexpression, the level of exosomal NAV2 appeared to increase sharply (Fig. 6E). To determine whether exosomal NAV2 is secreted from GP73-high hepatocytes in vivo, NAV2 expression in extracellular vesicle purified from the serum and liver of AAV-V and AAV-GP73 mice was analyzed. The abundance of exosomal NAV2 was increased by 2- to 4-fold in serum and liver tissue from AAV-GP73 mice (Fig. 6F-G). We next examined the clinical relevance of GP73 expression to the serum exosomal NAV2 level in CRLM patients. To this end, the GP73 and exosomal NAV2 levels were measured in serum from 6 CRLM patients. Notably, high serum GP73 was positively correlated with abundant exosomal NAV2 (Fig. 6H). Even more, NAV2 was found in close proximity to GP73 puncta in the livers of CRLM patients (Supplementary Fig. S6A).

Knockdown of liver NAV2 suppressed CRC liver metastasis in GP73-induced non-obese mice

To test whether exosomal NAV2 is transferred from GP73-high cells to cancer cells, MC38 cells were placed in the upper compartments of transwell chambers and incubated with AML-12 or GP73-high AML-12 cells in the lower compartments, without direct contact (Fig. 7A-B). Forty-eight hours later, MC38 cells in the upper compartments were analyzed. NAV2 was increased in the presence of GP73-high cells (Fig. 7C). Similarly, NAV2-GFP expression plasmid

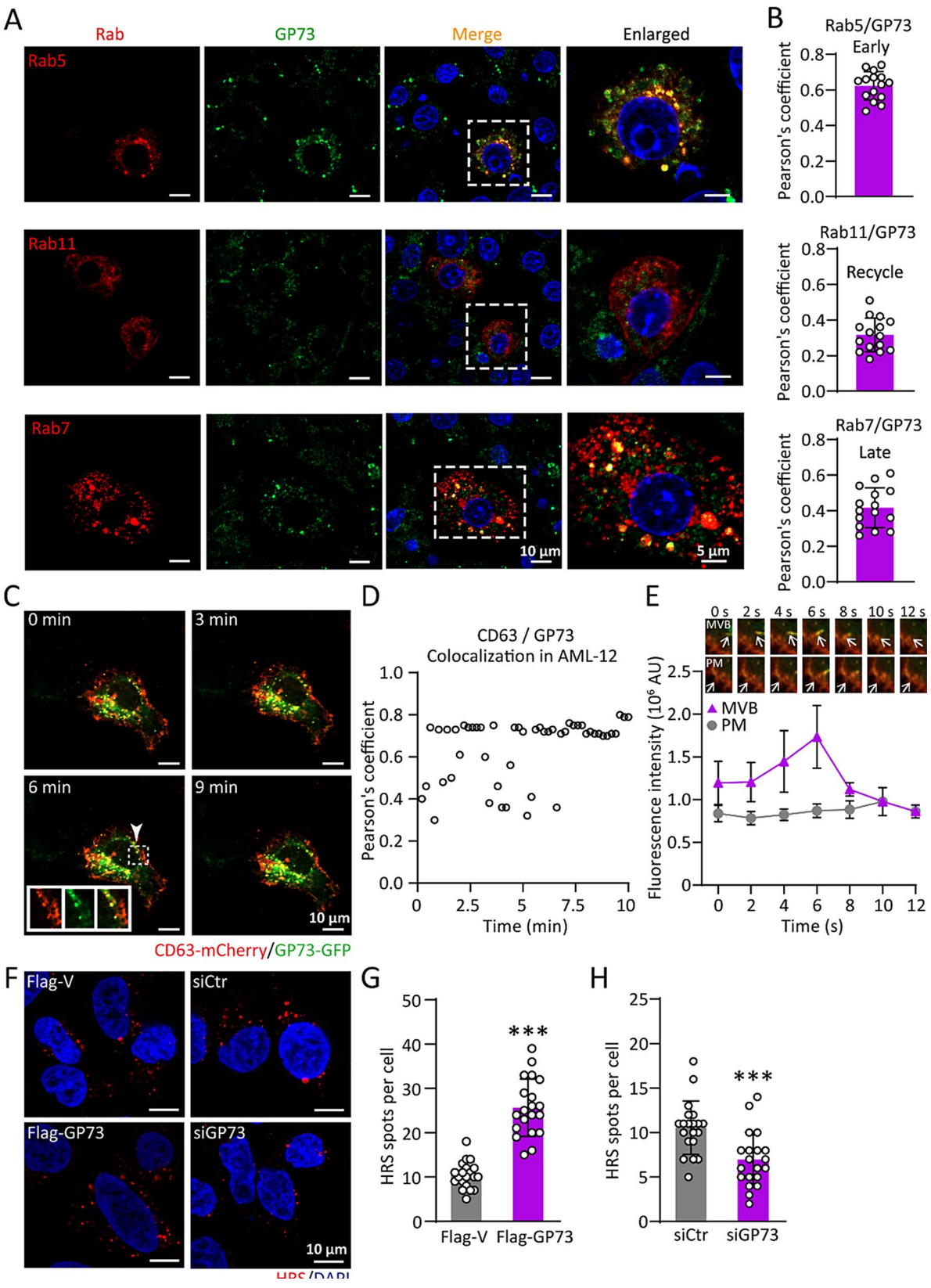

Fig. 3 (See legend on next page.)

(See figure on previous page.)

Fig. 3 GP73 overlaps with endosomal compartments and increases MVB numbers. (**A**-**B**) Confocal micrographs of GP73 (green) and markers of early (Rab5, red), recycling (Rab11, red), and late (RAB7, red) endosomes in AML-12 cells transfected with Flag-GP73 (**A**) and quantification of the Pearson's correlation coefficient for co-localization between GP73 and the endosome compartment ($n = 15$ cell fields; **B**). The scale bars represent 10 μm (whole image) and 5 μm (enlarged). (**C**-**E**) Confocal micrographs (**C**) and quantitative analysis (**D**-**E**) from live-cell imaging of AML-12 cells transfected with Flag-V or Flag-GP73. The white arrows show peripheral compartments where CD63 (red) and GP73 (green) co-localize; scale bar, 10 μm. Quantification of three independent experiments showing the range of Pearson's co-localization coefficient between GP73 and CD63 (**D**) and the mean ± SD fluorescence intensity inside the cell and in the plasma membrane (PM) (**E**) were automatically quantified (> 5 cells, 8 fields). (**F**-**H**) Confocal micrographs (**F**) and quantification of the MVB marker HRS in AML-12 cells transfected with Flag-V or Flag-GP73 (**G**) or transfected with control siRNA nucleotide oligoes (siCtr) or GP73 siRNA nucleotide oligoes (siGP73; **H**) ($n = 20$ cell fields). Each dot represents the number of HRS^+ particles from individual cells. Red, HRS staining; blue, nuclear DAPI staining; scale bar, 10 μm. Cell-based studies were performed independently at least three times with comparable results. All images were representative of three biological replicates. All quantitative data were presented as the mean ± SD. Statistical significance was determined using two-tailed Student's t test (**G**, **H**)

(pEGFP-N1-NAV2) was prepared and transfected to induce the expression of NAV2-GFP in Flag-GP73 293T and Flag-GP73 AML-12 cells. Fluorescence imaging and immunoblotting confirmed the transfer of GFP-tagged NAV2 from exosomes to tumor cells (Supplementary Fig. S7A-D). We then tried to test whether the transferred NAV2 was functional. Notably, exosomes from GP73-high AML-12 cells with NAV2 gene silencing markedly diminished the increases in the cell growth rates, migration, and invasion induced by exosomes from GP73-high cells (Fig. 7D-F). Meanwhile, we also tested the functional role of NAV2 in another CRC cell line CT26. Consistently, the cell growth and migration rates of CT26 cells were promoted by exosomes from GP73-high cells and markedly hampered by NAV2 gene silencing (Supplementary Fig. S7E-I).

We next sought to determine whether GP73-high hepatocytes can influence CRC liver metastasis by mediating distant communication through the secretion of NAV2-rich exosomes. To this end, we first generated mice with high liver GP73 expression by tail vein injection of AAV-V or AAV-GP73, as previously described. MC38 cells were injected intrasplenically 28 days after adenovirus injection to allow AAV-mediated GP73 expression in the liver (Fig. 7G). Compared with AAV-V mice, the liver-GP73-high animals developed slightly enlarged livers as well as increased lipid accumulation without a gain in body weight, consistent with the non-obese mice phenotype that we previously observed (Fig. 7H; Supplementary Fig. S7J). As expected, high levels of hepatocyte GP73 promoted the growth of metastasis, increasing the number of metastatic foci (Fig. 7I-K), while GP73 neutralizing antibody (GP73 Ab) treatment significantly blocked liver metastasis in GP73-induced non-obese MASLD mice (Fig. 7L-N). Importantly, the tumor metastasis growth and numbers was partially blocked in AAV-GP73 mice injected with siNAV2 to knock down hepatocyte NAV2 expression (Fig. 7O-Q; Supplementary Fig. S7K-L). Therefore, ExoGP73 enhance cancer cell invasiveness mainly through exosomal transfer of NAV2.

GP73 Blockade inhibits the increase in CRC liver metastasis triggered by HFD or HFrD feeding

A significant increase in dietary consumption of high fat or fructose levels has been implicated as a potential driver of cancer cell proliferation and metastasis, while the liver is the main organ that responds to changes in nutrition and orchestrates the systemic response to nutrition [44, 45]. Notably, we found that GP73 expression was dramatically induced in livers from mice fed on a HFD or HFrD for 4 months (Fig. 8A). Mice fed on a HFD or HFrD had significantly higher body weights, more severe liver steatosis, and more severely impaired blood glucose clearance than those fed on a RD, despite the fact that there were no significantly different cytokine profiles (Fig. 8A; Supplementary Fig. S8A-C). We next tried to link high liver GP73 expression with increased liver metastasis in this obese mouse model induced by HFD or HFrD feeding. No tumor or metastasis formation was observed in RD-fed mice 2 weeks after splenic inoculation, while 4/5 HFD-fed mice and 5/5 HFrD-fed mice exhibited metastasis (Fig. 8B; Supplementary Fig. S8D). Notably, no liver metastasis was observed in GP73 Ab-treated HFD-fed or HFrD-fed mice, (Fig. 8B-C; Supplementary Fig. S8D-E). We then injected siGP73 RNA interference (RNAi) nucleotide oligoes into HFrD-fed mice to determine whether knockdown GP73 in the liver affects liver metastasis. Notably, injection of GP73 siRNA nucleotide oligoes significantly decreased liver metastasis in 6 months HFrD-fed mice (Fig. 8D-G). Strikingly, siGP73 treatment significantly reduced NAV2 expression in the metastatic tumors (Fig. 8H-I). siGP73 injection also decreased the proliferation rate of metastatic tumor cells, as indicated by the reduced Ki67 staining (Fig. 8J; Supplementary Fig. S8F). Therefore, GP73 blockade inhibited the enhancement of CRC liver metastasis in obese mice triggered by HFD or HFrD feeding.

Discussion

In normal livers, GP73 is constitutively expressed in biliary epithelial cells but not in hepatocytes [46]. However, GP73 expression was found to be markedly upregulated in hepatocytes from patients with numerous liver

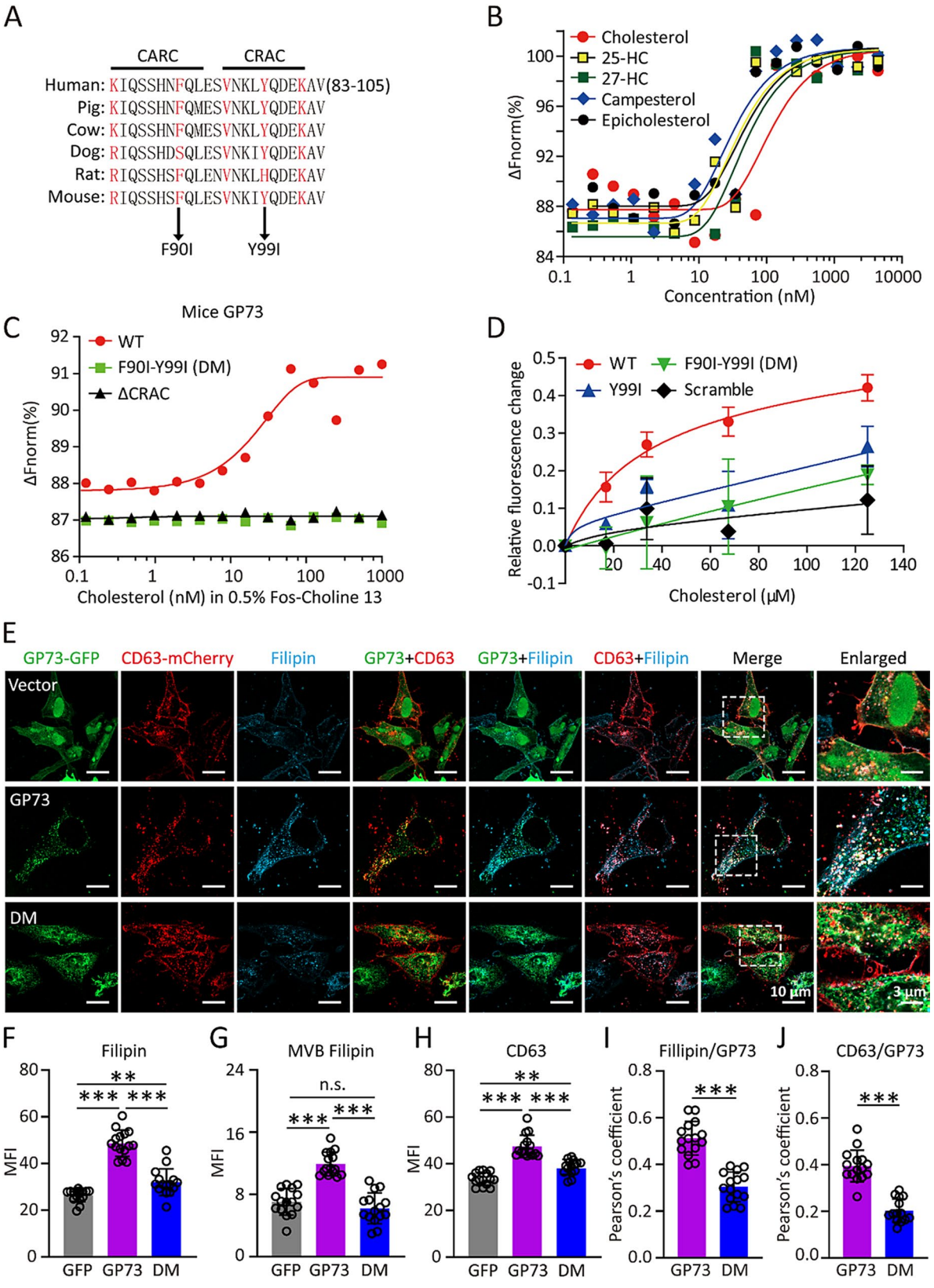

Fig. 4 (See legend on next page.)

(See figure on previous page.)

Fig. 4 GP73 binds to cholesterol and modulates the cholesterol content in MVBs. (**A**) Schematic illustration of the cholesterol-binding motif in GP73 in different species. Crucial amino acid residues in the CARC motif and CRAC motif are highlighted in red. (**B**) Analysis of interactions between GP73 and cholesterol, 25-HC, 27-HC, campesterol, and epicholesterol by MST. The data were derived from the effects of the indicated ligands on the fluorescence decay of fluorescently labeled GP73. (**C**) Analysis of interactions between cholesterol and mouse GP73 (WT), the GP73 CRAC domain deletion mutant (ΔCRAC) and the CARC Phe90/CRAC Tyr99 double mutant of mouse GP73 (F90I-Y99I, DM) by MST. The data were derived from the effects of the sterols on the fluorescence decay of fluorescently labeled proteins. (**D**) Titration curves showing changes in the intrinsic fluorescence of WT, Y99I, F90I-Y99I (DM), or scrambled peptides (5 μM) in the presence of increasing concentrations of cholesterol. (**E**-**J**) Confocal micrographs of CD63 and filipin staining in cells transfected with Flag-V, Flag-GP73, or Flag-DM (**E**) and quantitative mean fluorescence intensity (MFI) analysis of the filipin (**F**), filipin in MVBs (**G**), CD63 (**H**), and Pearson correlation coefficient for co-localization between filipin and GP73 (**I**) or GP73 and CD63 (**J**) ($n = 16$). Green, GP73-GFP; red, CD63-mCherry; cyan, filipin staining. **A** enlarged view of the boxed region is also shown. The scale bars represent 10 μm (whole image) and 3 μm (enlarged). Cell-based studies were performed independently at least three times with comparable results. All images were representative of three biological replicates. All quantitative data were presented as the mean ± SD. Statistical significance was determined using one-way ANOVA with the Bonferroni correction (**F**, **G**, **H**) or two-tailed Student's t test (**I**, **J**)

diseases, including virus-induced hepatitis (hepatitis B and C viruses), alcohol-induced liver disease, autoimmune hepatitis, liver cirrhosis, and HCC [46]. Here, we found significantly elevated GP73 expression in livers from CRLM compared with CRNLM and showed that high GP73 liver expression is critical for CRC liver metastasis in an exosome-dependent manner. Therefore, characterizing the biological features of GP73-high cells, especially their unique exosome secretion profiles, is highly important for delineating their roles in intercellular signal transduction. Here, we identified GP73 as a modulator of exosome biogenesis with a subsequent functional impact on tumor invasiveness. Mechanistically, high GP73 expression leads to higher abundance of ESCRT complex components (ALIX and TSG101) and tetraspanin CD63 that have been proven to be involved in the exosome biogenesis [47]; Moreover, GP73 upregulates a series of genes involved in cholesterol metabolism and trafficking pathways, binds cholesterol with high affinity, co-localizes with CD63-positive MVBs, and modulates the levels of free cholesterol in late endosome/MVB membranes. Exosomes derived from GP73-high hepatocytes contribute to the enhanced migratory ability of cancer cells that ultimately supports metastasis. The exosome biogenesis and increased cancer cell invasiveness by GP73-expressing hepatocytes was found to strictly require the cholesterol-binding ability of GP73. Specifically, we showed that GP73 induces cancer cell migration through exosomal NAV2 transfer. Importantly, we linked elevated GP73 liver expression with increased liver metastasis in the context of non-obese and obese MASLD and suggest that GP73 may serve as an effective molecular target to block cancer liver metastasis.

Cancer cells secrete more exosomes than healthy cells [48]. A higher abundance of exosomes has been detected in the plasma of cancer patients as well as in tumor cell cultures [49]. Previous results showed that GP73 had no obvious effect on the number of exosomes released from HCC cells. However, in the present study, we utilized multiple cell lines and clarified that GP73 significantly upregulates exosomal biogenesis. The consistent results in mice with global GP73 knockout supported the role of GP73 in exosomal production. However, our study did not specifically analyze whether GP73 influences the secretion of smaller or larger sized particles within the secretory vesicles of cells. Nonetheless, it remains plausible that GP73 could affect the profile of these secretory vesicles that are also known to play pivotal roles, and it represents a limitation of our research. Moreover, changes in the cholesterol levels can affect intracellular transport systems, such as the formation and maturation of endosomes and MVBs, which are important precursors of exosome formation. Abnormal cholesterol distribution and metabolism may disrupt the normal functions of these organelles, thereby influencing exosome formation and secretion. We demonstrated that the increased exosome production by GP73 is dependent on its ability to bind cholesterol. The observed GP73-MVB co-localization is compatible with a scenario in which a significant proportion of overexpressed GP73 is sorted into MVBs, in part for packaging into exosomes. Further investigation is required to better define the mechanistic details of the interplay between cholesterol trafficking and exosome biogenesis and downstream functions, in which GP73 appears to be a key player.

Intercellular communication roles played by exosomes is originated from their cargoes inside. Among the exosomal protein cargoes affected by GP73, NAV2 attracted our attention due to its central roles in cytoskeletal remodeling, microtubule dynamics and cell migration. The primary functional target of NAV2 in metastasis is the snail homolog 2 (SNAI2) protein, a member of a large superfamily of zinc finger transcription factors involved in cell adhesion and polarity defects and the enhancement of migration and invasion. NAV2 regulates SNAI2 ubiquitylation and degradation through the GSK-3β/β-catenin pathway [50]. In line with the key role of NAV2 in tumor metastasis, elevated expression of NAV2 has been associated with deeper invasion and with lymph node and distant metastasis in colorectal carcinoma and with unfavorable prognoses in multiple kinds of tumors [43]. NAV2 knockdown assays led to the reduced migration and invasion of cancer cells [43]. In this study, we found that NAV2 can be packaged into exosomes and that these

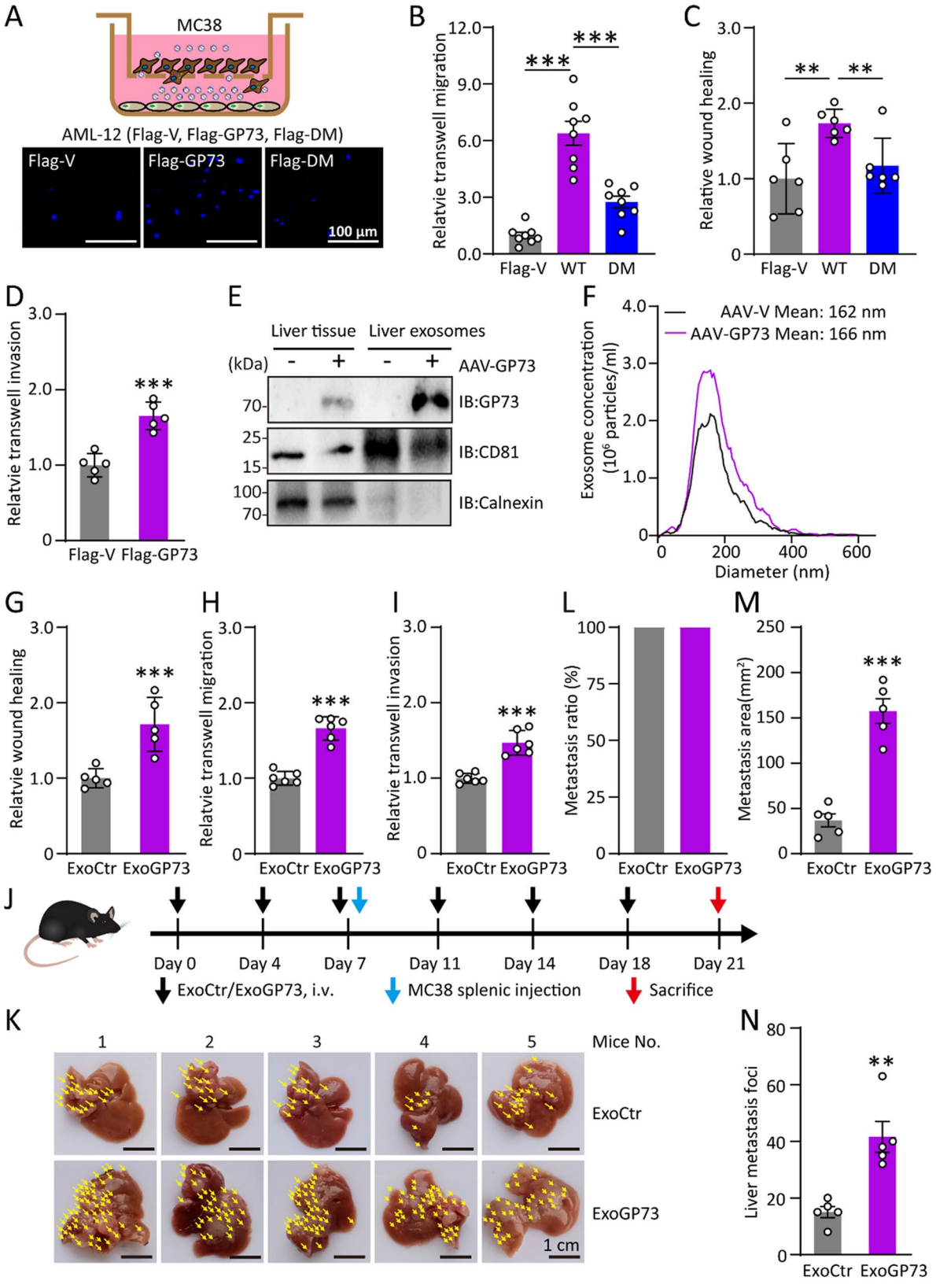

Fig. 5 (See legend on next page.)

(See figure on previous page.)

Fig. 5 Exosomes derived from GP73-high hepatocytes exert a prometastatic effect. (**A**) Schematic diagram of the Flag-V-, Flag-GP73- or Flag-DM-transfected cell co-culture system (upper) and representative images from transwell migration assay (lower). Scale bar, 100 μm. (**B**-**D**) Quantification of the transwell migration assay (**B**, $n=8$), the wound healing assay (**C**, $n=6$) and the Matrigel-transwell invasion assay (**D**, $n=5$) of the migrated MC38 cells in the co-culture system. The values in Flag-V-transfected AML-12 cells were set to 1. (**E**) Immunoblotting of exosome markers in liver lysates (10 μg of total protein) and purified in vivo-derived liver exosomes (10 μg of total protein). Molecular weights are shown to the left. (**F**) Representative NTA of purified liver exosomes from AAV-V- or AAV-GP73-injected mice. The x-axis shows the diameter of the vesicles, and the y-axis shows the concentration (10^6 particles/mL) of the vesicles. (**G**-**I**) Quantitative analysis of data from the wound healing assay (**G**, $n=5$), the transwell migration assay (**H**, $n=6$), and the Matrigel-transwell invasion assay (**I**, $n=6$) in migrated MC38 cells treated with ExoCtr or ExoGP73. The values in ExoCtr-treated MC38 cells were set to 1. (**J**) Schematic of the in vivo metastasis assay in mice treated with ExoCtr or ExoGP73 (2×10^8 particles/injection) twice a week ($n=5$ mice per group). (**K**-**N**) Representative images of metastatic liver tissue from mice inoculated with MC38 cells after treatment with ExoCtr or ExoGP73 ($n=5$ mice per group) (**K**) and quantification of metastatic tumor ratio (**L**), size (**M**), and number (**N**). The arrows show liver metastastic foci. Cell-based studies were performed independently at least three times with comparable results. All images were representative of at least three biological replicates. All quantitative data were presented as the mean ± SD. Statistical significance was determined using one-way ANOVA with the Bonferroni correction (**B**, **C**) or two-tailed Student's t test (**D**, **G**, **H**, **I**, **M**, **N**)

exosomes can deliver NAV2 into other cell types in the tumor microenvironment to regulate intracellular signaling pathways that affect cell migration via upregulation of intracellular GP73. Higher liver GP73 levels were accompanied by increased NAV2 expression in metastatic foci, and the abundance of exosomal NAV2 was found to be strongly connected with the serum GP73 level, further emphasizing the role of the GP73-NAV2 pathway in the context of liver metastasis.

Reported CRC metastasis research has shown that certain subgroups of circulating tumor cells were capable of metastasis [51]. In fact, the relationship among metastatic cancer cells, non-metastatic cancer cells, cancer stem cells, macrophages, and other cells at primary tumor sites are complicated. The migration and invasion rates of non-metastatic SW480 and Caco2 cells even could be increased in a dose manner in company with a certain degree of amoeboid phenotype changes which was conferred by the exosomes derived from metastatic SW620 cells; conversely, the exosomes shed by SW480 cells worked on their own or SW620 cells with no morphologic phenotype changes [52, 53]. The regulation of high GP73-induced NAV2-rich exosomes on non-metastatic CRC cells is elusive and needs to be further tested to enrich the knowledge of the GP73-NAV2 pathway. Additionally, future research should focus on that the high expression of GP73 in the liver may promote the metastasis of various tumors to different organs.

Obesity is associated with an increased incidence of primary and metastatic liver cancers [54]. Patients with MASLD have a marked predisposition to liver metastasis, with poorer overall survival [16]. While numerous mechanisms, including insulin resistance [55], inflammation, and hepatic lipids, have been implicated in liver metastasis [16], the way in which liver cells interact with distant or local tumor cells via exosomes is enigmatic [56]. After feeding of a HFD or HFrD, we observed increased GP73 levels in livers and an increased incidence of CRC metastasis, both of which were reversed by knockdown of GP73 expression in the liver. In addition, the presence of GP73 on exosomes can lead to amplified signaling via a positive feedback loop, effectively blocking the growth of colon cancer liver metastasis by neutralizing free circulating GP73 or GP73-harboring exosomes, a possibility that merits exploration as a potential therapeutic strategy for mitigating tumor cell metastasis to the liver.

GP73 is localized in the Golgi apparatus and is thus very likely to be closely related to the structure and functions of this organelle [57]. The Golgi apparatus relies on the constant influx of newly synthesized and recycled proteins from the ER for its maintenance [58]. The concentrations of Golgi proteins vary significantly between individual ER export sites, and Golgi ribbon architecture contributes to cell type-specific glycosylation patterns, as unlinked Golgi mini-stacks lead to differential enrichment of Golgi enzymes [59]. The observation that GP73 regulates increased exosomal sorting of ER membrane proteins and glycosylation enzymes may explain its intracellular roles in enhanced recycling through the ER resulting from the positioning of Golgi membranes at ER exit sites, a process that leads to dyshomeostasis of Golgi enzymes and altered glycosylation patterns. The ER stress induced by GP73 may result from this aberrant glycosylation. Therefore, as GP73 is a Golgi-resident protein containing ER retention signals, elucidation of its role in organizing the Golgi apparatus structure will help us to determine the multiple cellular functions of this protein implicated in various diseases. In conclusion, the findings in this study demonstrated that exosomes from GP73-high hepatocytes play important roles in liver metastasis progression, with GP73-induced exosomal NAV2 performing proinvasive functions in recipient cancer cells, thus endowing them with the ability to invade and metastasize. These results suggest a model for the mechanism by which GP73 reprograms the liver exosome profile and liver invasion of cancer cells. These findings might contribute to the development of novel therapeutic strategies for CRC liver metastasis in non-obese MASLD, obese MASLD or chronic GP73 liver upregulation for unknown reasons.

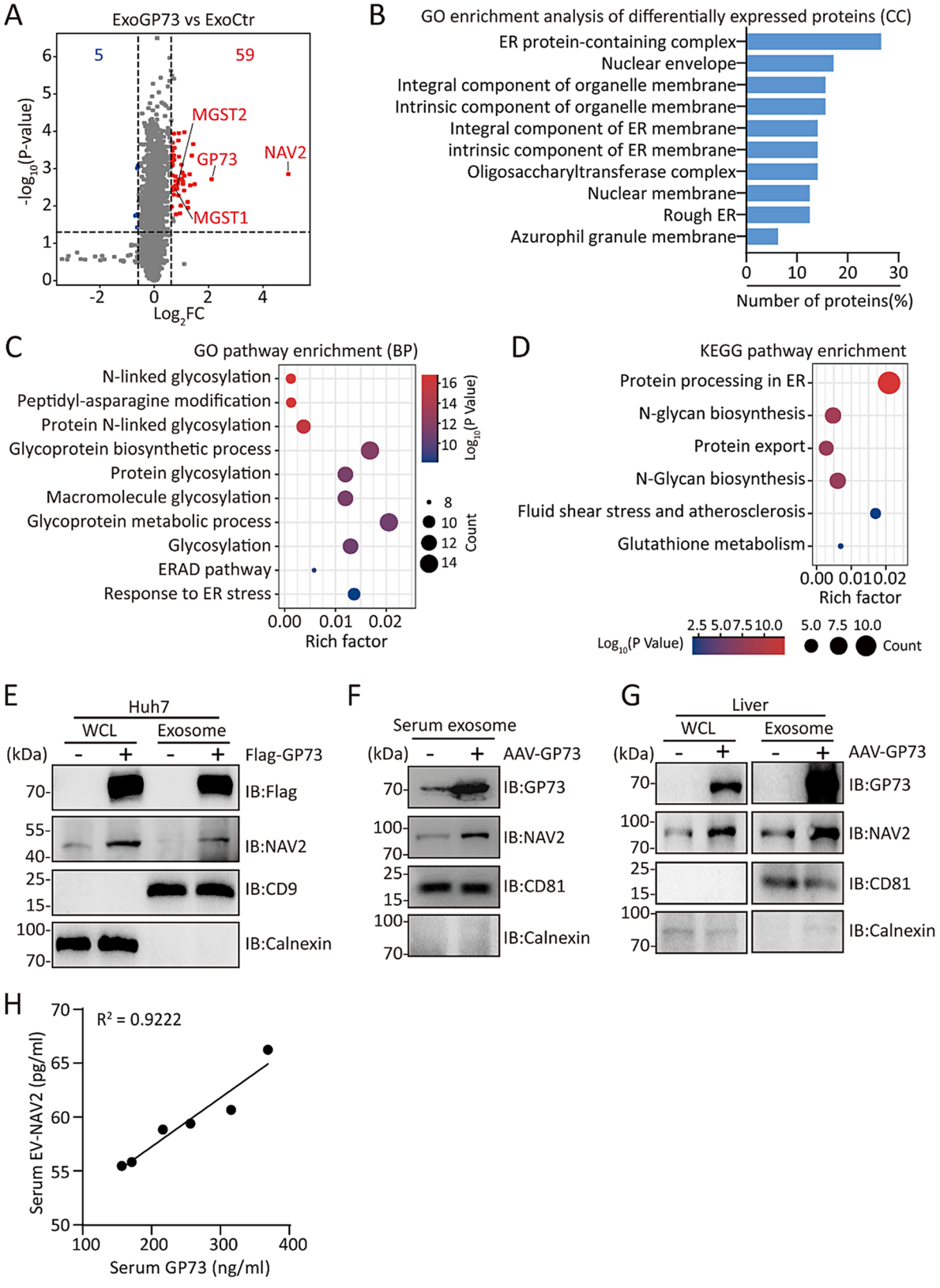

Fig. 6 (See legend on next page.)

(See figure on previous page.)

Fig. 6 GP73 mediates the production of NAV2-rich exosomes. (**A**) Volcano plot of protein abundances in exosomes derived from Flag-V- or Flag-GP73-transfected Huh-7 cells using LC-MS/MS-based proteomics. Significantly downregulated genes are shown in blue, and significantly upregulated genes are shown in red. The black vertical lines highlight fold changes (FCs) of -1.5 and 1.5, while the black horizontal line indicates a *P* value of 0.05. (**B**) Pathways enriched in ExoGP73 according to GO term analysis at GO cellular component (CC) level. The bar plot shows significantly percentage of dysregulated proteins in each cellular component. (**C**) Pathways enriched in proteins in ExoGP73 according to GO term analysis at the GO biological process (BP) level. The bar plot shows significantly dysregulated pathways, and Fisher's exact test *P* values are shown on the x-axis. (**D**) Pathways most significantly enriched in proteins in ExoGP73, according to KEGG pathway analysis. The enriched terms are shown on the y-axis, and the Fisher's exact test *P* values (log transformed) indicating the significance of enrichment are shown on the x-axis. The degree of KEGG pathway enrichment was quantified by the enrichment factor (rich factor), the *P* value and the number of genes enriched in the pathway. (**E**) Immunoblotting of NAV2, exosome markers (CD9) and negative marker of exosomes (Calnexin) in whole cell lysates (WCL) and in purified exosomes derived from Huh-7 cells transfected with Flag-V or Flag-GP73. Molecular weights (in kDa) are shown to the left. Anti-NAV2 antibody (Signalway Antibody) was used for the target of NAV2. (**F**-**G**) Immunoblotting of NAV2, exosome markers (CD81), and negative marker of exosomes (Calnexin) in serum exosomes (**F**) and liver lysates and purified liver exosomes from AAV-V- or AAV-GP73-injected mice (**G**) Molecular weights (in kDa) are shown to the left. Anti-NAV2 antibody (Affinity Biosciences) was used for the target of NAV2. (**H**) Pearson's correlation coefficients of the correlations between serum exosome NAV2 levels and GP73 levels in samples from CRLM ($n = 6$). Cell-based studies were performed independently at least three times with comparable results. All images were representative of three biological replicates

Materials and methods

Study subjects collection of clinical specimens and data

All patient specimens were obtained from Guangxi Medical University Cancer Hospital, and informed consent was obtained from each patient. Serum samples were collected from a total of 137 participants, consisting of 50 individuals undergoing physical examinations, 53 colon cancer patients without liver metastasis, and 34 colon cancer patients with liver metastasis. BMI was calculated as weight (kg) divided by height squared. Serum samples were collected to measure GP73 levels. Additionally, liver tissues from 4 healthy individuals and liver metastatic tissues from 8 colon cancer patients with liver metastasis were collected for immunofluorescence and RT-qPCR experiments.

Reagents

Dulbecco's modified Eagle's medium (DMEM-high glucose, D5796) was purchased from Millipore (Massachusetts, USA). Lipofectamine™ 2000 (11668027) was purchased from Invitrogen (California, USA). TransScript One-Step gDNA Removal and cDNA Synthesis SuperMix (AT311) and PerfectStart Green qPCR SuperMix (AQ601) were purchased from TransGen Biotech (Beijing, China). ELISA kits for human GP73 (SEB668Hu) and mouse GP73 (SEB668Mu) were purchased from Cloud-Clone (Wuhan, China) and ELISA kits for human serum GP73 were obtained from Hotgen Biotech (Beijing, China). Epicholesterol (R207349) were purchased from Sigma (St. Louis, USA). Fetal bovine serum (FBS, HY-T1000), cholesterol (HY-N0322), 25-hydroxycholesterol (HY-113134), 27-hydroxycholesterol (HY-N2371), campesterol (HT-N1459), filipin complex dye (HY-N6716), GW4869 (HY-19363), 4',6-diamidino-2-phenylindole (DAPI, HY-D1738) and PKH26 (HY-D1451) were purchased from MedChemExpress (Shanghai, China). Pre-stained protein markers were purchased from Thermo Fisher Scientific (Wilmington, USA) (26616) and LabLead (Beijing, China) (P1019). Goat serum (ZLI-9056) was purchased from Zhongshan Biotechnology (Beijing, China).

Antibodies

The anti-GP73 antibody (A02975-2, 1:1,000 dilution) was purchased from Boster Biological Technology (Wuhan, China). The rabbit anti-GP73 (15126-1-AP, 1:1,000 dilution), mouse anti-GP73 (66331-1-Ig, 1:1,000 dilution), anti-Ki-67 antibody (27309-1-AP, 1:5,000 dilution), CoraLite® Plus 647-conjugated HGS monoclonal antibody (CL647-67818, 1:1,000 dilution), anti-α-tubulin (11224-1-AP, 1:5,000 dilution), anti-E-cadherin (20874-1-AP, 1:2,000 dilution), anti-N-cadherin (22018-1-AP, 1:3,000 dilution), anti-SERPINE1 (66261-1-Ig, 1:5,000 dilution), anti-Vimentin (22031-1-AP, 1:1,000 dilution), anti-Snai1 (26183-1-AP, 1:1,000 dilution), anti-TWIST1 (25465-1-AP, 1:2,000 dilution), and anti-albumin (16475-1-AP, 1:100 dilution) antibodies were purchased from Proteintech (Wuhan, China). The anti-CD9 (EXOAB-CD9A-1, 1:1,000 dilution) and anti-CD81 (EXOAB-CD81A-1, 1:1,000 dilution) antibodies were purchased from System Biosciences (Palo Alto, USA). The anti-ALIX (ab275377, 1:1,000 dilution), anti-CD63 (ab134045, 1:1000 dilution), anti-TSG101 (ab125011, 1:1,000 dilution), and anti-calnexin (ab133615, 1:1,000 dilution) antibodies were purchased from Abcam (Cambridge, UK). The anti-GAPDH (RM2002, 1:1,000 dilution) antibodies were purchased from Ray Antibody Biotech (Beijing, China). The anti-Flag-HRP antibody (A8592, 1:1,000 dilution) was purchased from Sigma (St. Louis, USA). The anti-NAV2 antibody (DF9695, 1:1,000 dilution) was purchased from Affinity Biosciences (Nanjing, China). The anti-NAV2 antibody (46090, 1:500 dilution) was purchased from Signalway Antibody (Nanjing, China). The anti-Rab5 (PA5-29022, 1:100 dilution) and anti-Rab7 (PA5-52369, 0.25–2.00 μg/mL) antibodies were purchased from Thermo Fisher Scientific (Wilmington, USA). The anti-Rab11 antibody (Ys-6173R, 1:500 dilution) was purchased from Yaji Biological (Shanghai, China). The anti-rabbit HRP-IgG (ZB-2301, 1:5,000 dilution) and

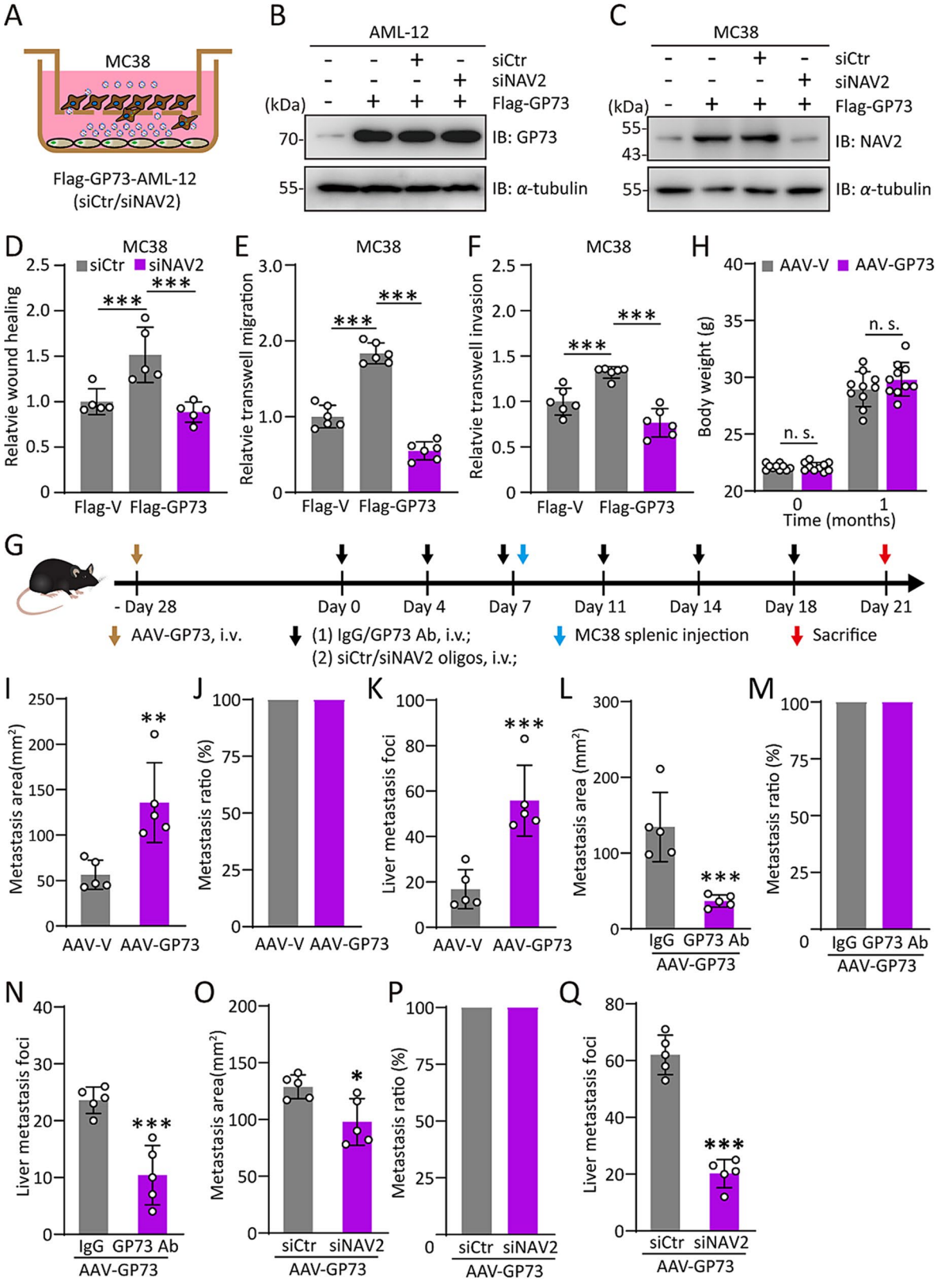

Fig. 7 (See legend on next page.)

(See figure on previous page.)

Fig. 7 Knockdown of liver NAV2 suppressed CRC liver metastasis in GP73-induced non-obese mice. (**A**) Schematic diagram of the co-culture system. Upper compartment: MC38 cells. Bottom compartment: Flag-V or Flag-GP73 AML-12 cells transfected with siCtr or siNAV2. (**B**-**C**) Immunoblotting analysis of NAV2 and GP73 protein in AML-12 cells (**B**) and MC38 cells (**C**) from the co-culture system. *α*-Tubulin was used as the loading control. Molecular weights (in kDa) are shown to the left. Anti-NAV2 antibody (Signalway Antibody) was used for the target of NAV2. (**D**-**F**) Quantification of the wound healing assay (**D**, $n=5$), the transwell migration assay (**E**, $n=6$), and Matrigel-transwell invasion assay (**F**, $n=6$) data for migrated MC38 cells co-cultured with Flag-V or Flag-GP73 cells transfected with siCtr or siNAV2. The values in Flag-V-AML-12 cells transfected with siCtr were set to 1. (**G**) Schematic of the in vivo metastasis assay in AAV-V- and AAV-GP73-treated mice injected with GP73 Ab or siNAV2 RNAi nucleotide oligoes twice a week beginning at 4 weeks after adenovirus injection ($n=5$ mice per group). (**H**) Body weights of AAV-V- and AAV-GP73-treated mice ($n=10$ mice per group). (**I**-**K**) Quantification of metastatic tumor size (**I**), ratio (**J**), and number (**K**) of AAV-V- and AAV-GP73-injected mice. (**L**-**N**) Quantification of metastatic tumor size (**L**), ratio (**M**), and number (**N**) of AAV-GP73-injected mice in the presence of mouse IgG or anti-GP73 antibody (15 mg/kg mouse IgG or GP73 Ab). (**O**-**Q**) Quantification of metastatic tumor size (**O**), ratio (**P**) and number (**Q**) of AAV-GP73-injected mice injected with siCtr or siNAV2 RNAi nucleotide oligoes (60 nmol/kg). Cell-based studies were performed independently at least three times with comparable results. All images are representative of three biological replicates. All quantitative data are presented as the mean ± SD. Statistical significance was determined using one-way ANOVA with the Bonferroni correction (**D**, **E**, **F**) or two-tailed Student's t test (**H**, **I**, **K**, **L**, **N**, **O**, **Q**)

anti-mouse HRP-IgG (ZB-2305, 1:5,000 dilution) secondary antibodies were purchased from ZSGB-BIO (Beijing, China). Cy3 conjugated Goat Anti-Rabbit IgG (GB21303, 1:100 dilution), Cy3 conjugated Goat Anti-Mouse IgG (GB21301, 1:100 dilution), Alexa Fluor 488 conjugated Goat Anti-Rabbit IgG (GB25303, 1:100 dilution), and Alexa Fluor 488 conjugated Goat Anti-Mouse IgG (GB25301, 1:100 dilution) antibodies were purchased from ServiceBio (Wuhan, China). GP73 neutralizing antibody (GP73 Ab) and mouse IgG antibody were prepared by Hotgen Biotech (Beijing, China).

Plasmids and cell culture

N-terminal Myc-tagged and C-terminal Flag-tagged GP73 expression plasmids were constructed by inserting the corresponding PCR-amplified fragments into pcDNA3.1 (V79520; Invitrogen, USA). The pcDNA3.1-Flag-DM and CRAC deletion mutant sequences were constructed with a Tiangen Fast Site-Directed Mutagenesis Kit (Beijing, China). Primers were designed accordingly and used to amplify the target DNA segments of the human and mouse gp73 genes by PCR. The CD63-mCherry expression plasmid pCMV-CD63-mCherry was purchased from Beyotime (Shanghai, China). GP73-GFP (WT and DM) and pEGFP-N1-NAV2 (NAV2-GFP) expression plasmids were prepared on the base of pEGFP-N1 (GFP-V) (purchased from MiaolingBio, Wuhan, China). The cDNA of human NAV2 gene (NM_145117) was introduced at the *Xho*I / *Eco*RI sites of pEGFP-N1 to construct the pEGFP-N1-NAV2 expression plasmid that can produce the recombinant hNAV2 protein tagged with a C-terminal GFP. The AML-12 (CRL-2234), 293T (CRL-3216) cell lines were obtained from the American Type Culture Collection (ATCC; Rockville, USA). The MC38 (CL0203), and CT26 (CL0863) cell lines were purchased from Fenghui Biotech (Changsha, China). The Huh-7 (0403) cell line was obtained from the Japanese Collection of Research Bioresources. All cell lines were tested for mycoplasma contamination and were incubated in DMEM media at 37 °C in a humidified atmosphere with 5% CO_2. Lipofectamine™ 2000 was used for vector transfection following the manufacturer's protocol.

Animals

Male C57BL/6 N wild-type mice (8-week old), purchased from SPF Biotechnology (Beijing, China), were conventionally group-housed on a 12-h light/dark cycle in an animal facility for 3 days before any procedures were performed.

For adeno-associated virus (AAV) injection, AAV-GP73 encoding mouse GP73 and AAV-vector (AAV-V) were constructed and propagated by Hanbio, Inc. (Shanghai, China). The mice were injected intravenously with 3×10^{11} vg per capita.

For the GP73-KO mouse model, it was generated using CRISPR/Cas9 technology. Two sgRNAs targeting exon 4 of the GP73 gene (gene ID: 105348) were designed using the online tool (http://crispor.tefor.net/), specifically targeting transcript ENSMUST00000022039.6. The sgRNAs (5'-CTGGACAAGCCTTCATCCCTTGG-3' and 5'-TG CCTTCTGACCTTGGCCTGAGG-3') were co-injected with Cas9 mRNA into fertilized C57BL/6 N mouse zygotes, which were then implanted into pseudopregnant females. Positive founder (F0) mice were identified by PCR and sequencing using primers (P1: 5'-GTCACA ACGAAGCCGACTGACCTACAT-3' and P2: 5'-GCG AGTTTCAGGACAGTTAAGGCTGC-3'). The F0 mice were bred with wild-type mice to obtain F1 heterozygous ($GP73^{-/+}$) mice, which were interbred to produce homozygous $GP73^{-/-}$ mice. Littermates of wild-type C57BL/6 N mice were used as controls. Knockout validation was confirmed by immunoblotting analysis using an anti-GP73 antibody.

To establish the nutrition-induced model, all the mouse diets were purchased from BiotechHD Biotech (Beijing, China). Male C57BL/6 N mice were fed on a regular diet (RD, HDS01), or high fat diet (HFD, HD001b) or high fructose diet (HFrD, HD016) for at least 4 months. For glucose tolerance tests (GTT), mice were fasted for 6 h followed by the delivery of a bolus of glucose (1.5 g/kg body weight) into the stomach by a curved feeding needle

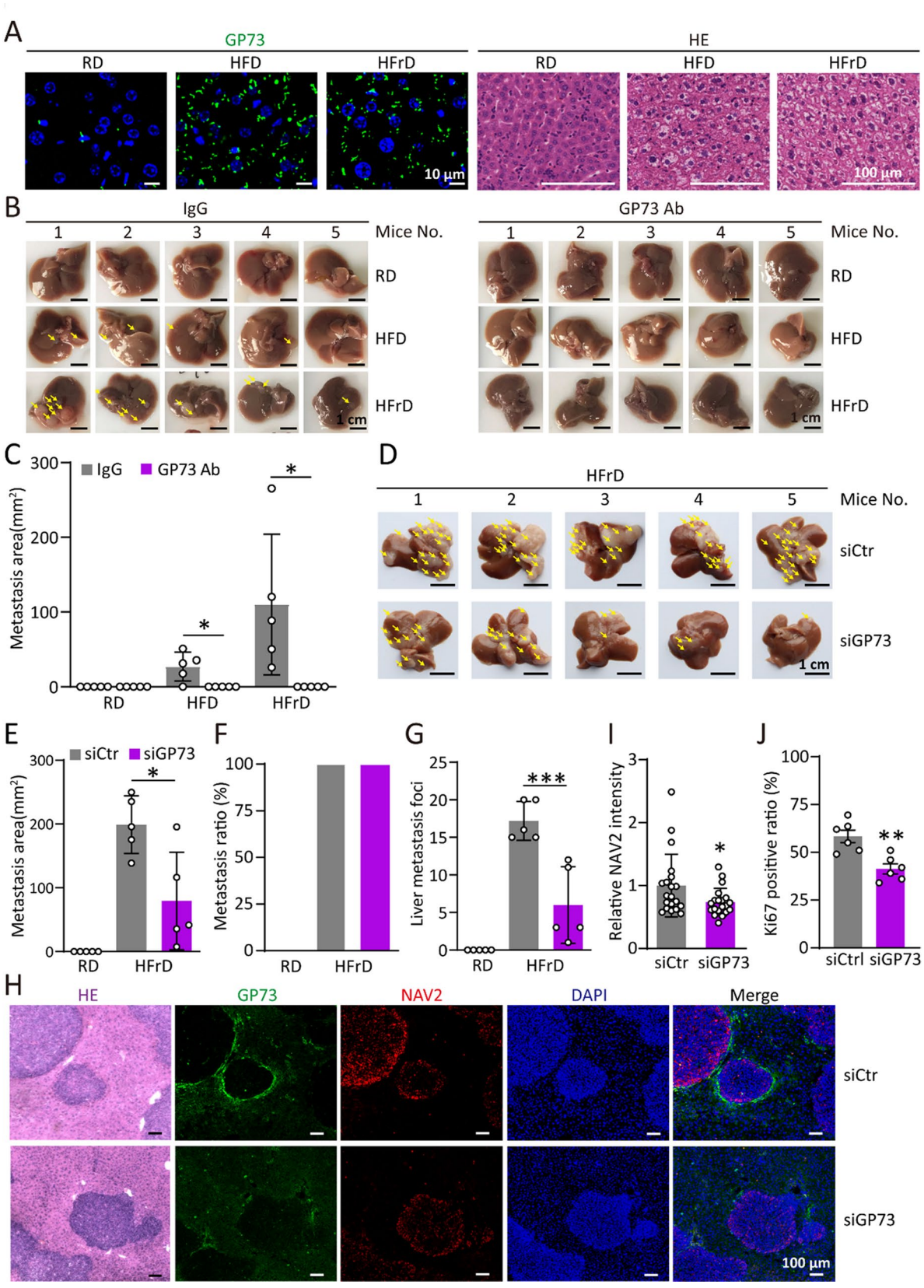

Fig. 8 (See legend on next page.)

(See figure on previous page.)

Fig. 8 GP73 blockade inhibited the increase in CRC liver metastasis triggered by HFD or HFrD feeding. (**A**) Representative images of GP73 staining (**A**; scale bars, 10 μm) or HE staining (scale bars, 100 μm) in livers from mice fed on a RD, HFD, or HFrD for 4 months ($n = 5$ mice per group). Green, GP73 staining; blue, nuclear DAPI staining. (**B**-**C**) Representative images of metastatic liver from mice fed on a RD, HFD or HFrD for 4 months and inoculated with MC38 cells via intrasplenic injection after the treatment of mouse IgG or GP73 Ab (**B**, $n = 5$ mice per group; 15 mg/kg) and quantification of metastatic tumor size (**C**). (**D**-**G**) Representative histopathological images of metastatic liver tissue from siCtr- or siGP73-treated mice fed with HFrD for 6 months and inoculated with MC38 cells via intrasplenic injection (**D**, $n = 5$ mice per group) and quantification of metastatic tumor size (**E**), ratio (**F**), and numbers (**G**). (**H**-**J**) Representative immunofluorescence staining images of metastatic tissue from siCtr- or siGP73-treated mice fed with HFrD (**H**) and quantification of the relative NAV2 (**I**) and Ki67 (**J**) staining for each group, based on 20 and 6 independent fields, respectively. Green, GP73 staining; red, NAV2 staining; blue, DAPI staining. Scale bars, 100 μm. The arrows show liver metastastic foci. All images are representative of three biological replicates. Anti-NAV2 antibody (Affinity Biosicences) was used for the target of NAV2. All quantitative data are presented as the mean ± SD. Statistical significance was determined using two-tailed Student's t test (**C**, **E**, **G**, **I**, **J**)

(20-gauge); Blood glucose was collected and measured from the tail vein by tail snipping at 0, 15, 30, 60, 90, and 120 min post glucose delivery. For the quantification of serum cytokines, mice sera samples were measured using a custom 36-plex mouse ProcartaPlex Luminex panel (Thermo Fisher Scientific, EPXR360-26092-901) following the manufacturer's instructions in Bio-Plex MAGPIX multiplex reader (Bio-Rad) and analyzed by Bio-Plex Manager software (version 6.1).

To establish the syngeneic xenograft mouse model, the MC38 cell suspension was diluted to a concentration of 1×10^6 cells/100 μL and proper mixing was ensured. Then, the C57BL/6 N mice were anesthetized by administration of the anesthetic according to the appropriate protocol. The surgical area was sterilized, and aseptic conditions were maintained throughout the procedure. An incision was made in the abdominal area to expose the spleen. Then, aliquots of the 100 μL MC38 cell suspension were carefully injected into the mice spleens using a syringe and a fine needle followed by the removal of total spleens. The incision site was then sutured or sealed to prevent leakage or infection. Mice were observed for any signs of distress or complications after surgery, and appropriate care was provided. Then they were sacrificed for collection of plasma and liver tissues at the indicated times. Metastatic foci on the surface of mice livers were counted and recorded by cameras. The metastatic foci areas were measured by ImageJ. All samples were snap frozen in liquid nitrogen and stored at -80 °C until analysis.

For the application of exosomes, ExoGP73 or ExoCtr was administered at a dose of 2×10^8 particles/injection, 200 μL per mouse via tail vein injection twice a week. To block the effect of GP73, siGP73, siNAV2 or the corresponding control siRNA nucleotide oligo was administered at a dose of 60 nmol/kg to the mice via tail vein injection twice a week. By the same way, GP73 neutralizing antibody or mouse IgG was administered at a dose of 15 mg/kg to the mice twice a week. After a specified period, mice were sacrificed for liver metastasis analysis.

CCK-8 assays

Cells were first counted, and approximately 4000 cells per well were seeded in a 96-well cell culture plate (Service-Bio, Wuhan, China). Then, after incubation at 37 °C in a humidified atmosphere with 5% CO_2 for 24 h, the culture medium was replaced by a series of concentrations of drugs. Six replicates were made for each measurement. Finally, a total amount of 10 μL of Solarbio CCK-8 reagent solution (CA1210; Beijing, China) and 100 μL of DMEM without phenol red was added to each culture well and incubated for 4 h. When CCK-8 was reduced to formazan pigment by living cells, 100 μL of the assay medium was transferred to a new 96-well plate, and the absorbance at 450 nm was measured in a Tecan Spark multifunction microplate reader (Männedorf, Swiss).

Immunoblot analysis

The cultured cells or tissues used for immunoblotting were lysed and centrifuged at 4 °C for 15 min at 13,000 × *g*, and the proteins in the supernatants were separated by using sodium dodecyl sulfate-polyacrylamide gel electrophoresis (SDS-PAGE) after centrifugation. The separated proteins were then transferred to polyvinylidene fluoride (PVDF) membranes for immunoblot analysis using the indicated primary antibodies. Digital images were analyzed using AlphaView software or ImageJ. The band intensities representing the indicated relative expression levels were quantitated with reference to the α-tubulin band intensities and the corresponding protein levels in the control group.

Quantitative real-time PCR (RT-qPCR)

Total mRNA was extracted using NucleoZOL (740404.200; Düren, Germany). cDNA was prepared from total mRNA using TransScript One-Step gDNA Removal and cDNA Synthesis SuperMix. The relative expression levels of individual mRNAs were calculated after normalization to the GAPDH mRNA level in the corresponding sample as previously described. The primer for amplification of GP73 and GAPDH were obtained from Tsingke Biotech (Beijing, China) and listed below:

GP73-F: GAGAAGCTCATTCGAGACCTG.
GP73-R: ATCTGGCTGATACACTGGTTC.
GAPDH-F: AGGTCGGTGTGAACGGATTTG.
GAPDH-R: TGTAGACCATGTAGTTGAGGTCA.

Chemical modifications of siRNAs for in vivo study

RNA interference (RNAi) nucleotide oligoes for NAV2 and GP73 were obtained from GenePharma (Shanghai, China). Gene knockdown was performed by using siRNA nucleotide oligoes, the efficiency of which was calculated based on the ImageJ quantified band intensities of immunoblotting images. In the sense strand of each siRNA nucleotide oligo, the 3' terminus was modified by cholesterol and 4 thiol moieties, the 5' terminus was modified by 2 thiol moieties, and the whole strand was modified by 2'-O-methylation. The siRNA sequences are listed below:

siGP73: 5'- CCUGGUGGCCUGUGUUAUUTT – 3'.
siNAV2: 5'- AAGGACTCCAGCTCTACGGTT – 3'.
Scrambled siRNA nucleotide oligoes corresponding to siGP73 and siNAV2 were used as controls (siCtr).
siCtr(GP73): 5'-UUCUCCGAACGUGUCACGUTT-3'.
siCtr(NAV2): 5'-ACGUGACACGUUCGGAGAATT-3'.

Microscale thermophoresis (MST)

To produce proteins for binding studies, the human and mouse GP73 cDNA sequences were inserted into the pcDNA3.1 vector with a 6-His tag on the N-terminus. His-GP73 protein from 293T cells transfected with the above plasmids was first bound to a Ni-NTA His-Bind column (GE Healthcare, USA) and was purified by size exclusion columns and polymyxin B-based endotoxin-depletion columns. The final His-GP73 proteins used in all experiments featuring recombinant proteins had a purity of > 90% (endotoxin < = 2 EU/mL) and were then labeled with NT-647 dye for 30 min at room temperature using the Monolith His-Tag Labeling Kit (NanoTemper Technologies, MO-L008). The binding buffer of 50 mM Tris-HCl (pH 7.5), 150 mM NaCl, 1 mM dithiothreitol (DTT), and 0.5% (*v*/*v*) fos-choline 13 was used as the negative control. The concentrations of cholesterol and cholesterol derivatives used for the 16-step, 2-fold dilution curves ranged from 4 μM to 122 pM. Dry powders of cholesterol and other sterols were mixed with binding buffer at 25 °C and incubated with gentle agitation for 3 h. A dilution of cholesterol or cholesterol derivatives was then added to the labeled protein (100 nM final concentration) in binding buffer at room temperature. Samples were loaded into standard glass capillaries (NanoTemper Technologies, MO-K022). Three independent MST experiments were performed on a Monolith NT.115 instrument (NanoTemper Technologies). Control software with settings of 60–80% excitation power and 40% MST power at room temperature.

Peptide-cholesterol binding assay

The synthetic peptides were ordered from SciLight-Peptide Biotechnology (Beijing, China). A peptide (assigned as "Scrambled") with a random amino acid sequence was used the negative control and the N-terminal and C-terminal Lys residues increase the solubility of the hydrophobic CARC-CRAC transmembrane segment. Replacing the Glu residue with Trp between the CARC and the CRAC motifs conferred intrinsic fluorescence upon excitation at 280 nm, with maximum emission at 350 nm. Peptides (5 mM) in dimethyl sulfoxide (DMSO) were diluted to a final concentration of 5 μM in assay buffer containing 140 mM NaCl and 20 mM Tris (pH 8.5) supplemented with 2 mM tris (2-carboxyethyl) phosphine (TCEP) and 2% (*v*/*v*) ethanol. Cholesterol in ethanol was diluted to final concentrations ranging from 0.5 to 50 μM in 500 μL volumes of peptide solution. These dilutions were incubated overnight at 25 °C with gentle agitation. A Cary Eclipse fluorescence spectrophotometer (Agilent Technologies), with excitation and emission wavelengths of 280 and 350 nm, respectively, was used for fluorescence measurements. All measured fluorescence values fell within the linear range of the instrument. Fluorescence intensity values were averaged and are expressed as relative changes with respect to the 0 μM ligand condition. The data were fitted to saturation binding equations using GraphPad Prism 8.0. The dotted lines indicate regions where the data could not be fitted.

Exosomes

Cells indicated for exosome preparation were transfected with the indicated vectors. Culture medium supernatants of those cells were pooled and centrifuged sequentially at 300 × *g* (10 min at 4 °C), 2,000 × *g* (20 min at 4 °C) and 10,000 × *g* (30 min at 4 °C). The supernatants were filtered through a 0.22 μm filter membrane, then transferred to ultracentrifugation tubes and further centrifuged at 100,000 × *g* (80 min at 4 °C). After centrifugation, the exosome pellets were suspended in PBS and collected again by ultracentrifugation at 100,000 × *g* (80 min at 4 °C). The resulting exosome pellets were suspended in PBS. Mice serum exosomes were isolated and purified according to the Umibio commercial kit manual (UR52151; Shanghai, China). In brief, serum exosomes were isolated by the size exclusion chromatography purification method. To this end, 100 μL of serum was added to the SEC purification column for natural discharge, the effluents were discarded, 200 μL of PBS was added to the SEC purification column for elution, and the effluents were naturally discharged. The effluents were the exosomes. For the extraction of exosomes from liver tissues, each liver tissue sample weighed approximately 100 mg with a volume of about 0.1 cubic centimeters after the mice were sacrificed. The collection was started within

5 minutes' post-euthanasia to ensure sample consistency and quality. The detailed procedures were shown in the supplementary document. Briefly, sliced liver tissues were digested by collagen enzyme at 37°C for 30 min followed by the filtration through 70 μm cell strainers. Then the tissue plasma was centrifuged sequentially at 500 × *g*, 3,000 × *g*, 10,000 × *g*, and 100,000 × *g*. The resulting exosome pellets were finally suspended in PBS. Exosome samples were snap frozen in liquid nitrogen and stored at − 80 °C until analysis. The total protein concentration in the isolated exosomes was measured with a bicinchoninic acid (BCA) protein quantification kit (Thermo Fisher Scientific, USA). The morphology of isolated exosomes was assessed by transmission electron microscopy. In brief, samples were embedded on an electron-transparent sample support (EM grid), and then 1% phosphotungstic acid was used for negative staining. To determine the exosome nanoparticle size, ZetaView (Particle Metrix, GER) was applied. The exosome markers CD9, CD63, CD81, and TSG101 were analyzed by immunoblotting after loading of equal amounts of exosomal particles. For the assessment of exosome internalization, ExoCtr and ExoGP73 exosomes were stained with PKH26 dye following the manufacturer's instructions and then incubated with MC38 cells for microscopy observation and fluorescent intensity analysis by ImageJ.

Nanoparticle tracking analysis (NTA)

Exosome samples were diluted in PBS to a final volume of 1 mL and analyzed using a Malvern Panalytical NanoSight NS300 (Malvern, UK) with a 488 nm laser (Blue) and a scientific CMOS camera. For each measurement, three consecutive videos were recorded under the following parameters: camera level 13, detection threshold 5, capture duration 60 s, capture rate 25 frames per second, temperature 25°C, and syringe pump speed 22 μL/s (100 AU). Bioss Dulbecco's phosphate-buffered Saline (DPBS, C7163, Beijing, China) was used as a negative control and Applied Microspheres standard nano-particles (10100-20, Germany) as the positive control. After capture, data analysis was achieved by using the built-in Malvern Panalytical NanoSight Software NTA 3.3.301 (Malvern, UK).

Transmission electron microscopy

For morphological observation by transmission electron microscopy, 3–5 μL of an exosome suspension was adsorbed onto a copper mesh applied to ultrathin carbon foil (230 mesh size). The suspension was allowed to adsorb for 1 min at room temperature. Absorbent paper was used to gently remove excess liquid. Then, 3–5 μL of 2% uranyl acetate was added to the copper mesh, and absorbent paper was used to gently remove excess liquid This process was repeated twice, and 3–5 μL of 2% uranyl acetate was then added and incubated for 1 min. Excess liquid was again absorbed with absorbent paper. The copper mesh was air-dried and examined using a Tecnai Spirit 120 kV transmission electron microscope (Thermo Fisher Scientific, USA).

Hematoxylin-eosin (HE) staining

Tissues were fixed with 4% (*w*/*v*) paraformaldehyde (PFA) solution at 4 °C overnight and embedded in paraffin, and 5 μm-thick sections were prepared. Paraffin sections were rehydrated and stained with hematoxylin and eosin sequentially.

Immunofluorescence staining

For immunofluorescence staining, sections were heated in an autoclave in citrate buffer (12 mmol/L, pH 6.0), and blocked for 30 min with 10% (*v*/*v*) goat serum. The sections were subsequently incubated with primary antibodies at 4 °C overnight, then incubated with secondary antibodies for 1 h at room temperature, washed and stained with 10 μg/mL of DAPI. Images were captured with a confocal fluorescence microscope (Zeiss LSM 800, Carl Zeiss Microscopy GmbH, Jena, Germany) or an automatic digital slide scanner (Pannoramic MIDI, 3D HISTECH, Budapest, Hungary). The immunofluorescent signals in images were measured by ImageJ and JACoP.

For cell cover slip preparation, GP73-GFP expression plasmids were tranfected into host cells for target protein expression. The cover slips were washed three times in PBS and then immersed in 4% (*w*/*v*) PFA for 15 min. The cover slips were then washed three times in PBS. The samples were blocked with 10% (*v*/*v*) goat serum and were then incubated with primary antibodies overnight at 4 °C. Cy3 Conjugated secondary antibody (1:100 dilution) was incubated with the samples for 30 min at 37 °C. Intracellular cholesterol was stained using Filipin complex dye [60]. Cells were visualized using a laser confocal microscope and filter sets appropriate for the labels used.

Live cell imaging

For live visualization of intracellular mobility, Cells were grown in 12-well plates at a density of 2×10^5 cells per well in duplicates. After the 24 h co-transfection of GP73-GFP expression plasmid and CD63-mCherry expression plasmid, imaging was performed on a Dragonfly 200 confocal microscope system (Oxford Instruments, UK) at 37 °C and 5% CO_2 in growth medium. A 60× objective was used to acquire images at high resolution. At each location and time point, the Z focus was determined by means of image autofocus. Acquisition parameters were set to limit photodamage for each channel (488 nm and 561 nm) during the courses of 30 min experiments while having sufficient signal-to-noise ratio. The resulting images containing the time frames of each fluorescence channel were stacked as Imaris image files with a frame

rate of 2 s/frame. Videos and images were edited and exported by Imaris Viewer x64 (Oxford Instruments) in order to focus on time frames and fields of interest.

Wound healing assays

Approximately 5×10^5 cells/well were plated in a 6-well plate. When the convergence reached around 80%, wounds were created by scratching the monolayer surface using a sterile 10-μL pipette tip. Cells were cultured in serum-free DMEM media with the addition of 3×10^8 exosomes/well. The plates were photographed using an Nikon ECLIPSE Ti2-U inverted microscope and the gaps were measured using ImageJ software.

Transwell assays

For invasion assays, the upper Transwell compartments of 24-well plates (8-μm pore polyester membrane) was coated with 8 mg/mL Matrigel (356234, Corning) for filtering and pretreated for 2 h in serum-free DMEM medium at 37 °C, 5% CO_2. AML-12 cells were grown in DMEM medium with 10% FBS in 6-well plates, and transfected with different GP73 expression plasmids or siRNA nucleotide oligoes. After transfection for 12 h, the cells in 6-well plates were re-plated into the lower Transwell compartments of 24-well plates with 1.5×10^4 cells/well and 2×10^3 cells/well tumor cells were plated in the upper compartments. Cell status was observed after coculture for 48 h. Cells on the upper surfaces of the upper compartments were removed and the lower surface cells were fixed with 4% PFA for 30 min, stained with DAPI for 30 min, and photographed under the microscope. Observation fields were captured and cell numbers were measured using ImageJ software.

For migration assays, a procedure similar to the invasion assays was performed using the upper compartments without Matrigel.

Sample preparation for proteomic analysis

Exosome samples were sent to Shanghai Luming Biological Technology (Shanghai, China) for quantitative proteomic analysis. Exosomes derived from cells were transferred into low-protein-binding tubes and lysed with 300 μL of lysis buffer supplemented with 1 mM PMSF. Then, the samples were further lysed by sonication. The parameters were set as follows: 1 s/1 s intervals, 80 W, 2 min. After sonication, the samples were centrifuged at 12,000 rpm for 10 min at 4 °C to remove insoluble particles, and this step was repeated to further prevent precipitation. The protein concentration was determined by a BCA assay. Based on the measured protein concentration, equal amounts of protein were taken from each sample, and the samples from different groups were diluted to the same concentration and volume. The corresponding volume of 25 mM DTT was added to the above protein solutions to a final DTT concentration of approximately 5 mM, and the solutions were incubated at 55 °C for 30 min. Then, the corresponding volume of iodoacetamide was added to a final iodoacetamide concentration of approximately 10 mM, and the samples were placed in the dark for 15 min at room temperature. Then, a 6-fold volume of precooled acetone was added to the above systems to precipitate proteins, and the samples were incubated at -20 °C for more than four hours or overnight. Subsequently, the samples were centrifuged at 8000 × g for 10 min at 4 °C to collect the precipitates. Based on the amount of protein in the samples, the corresponding volume of enzymolysis diluent (protein: enzyme = 50:1 (m/m), 100 μg of protein added to 2 μg of enzyme) was added to redissolve the protein precipitate, and the solutions were then incubated for digestion at 37 °C for 12 h. Finally, the samples were lyophilized or evaporated after enzymolysis.

Tandem mass Tag (TMT)-based isobaric labeling

For TMT labeling, lyophilized samples were resuspended in 100 μL of 200 mM triethylammonium bicarbonate (TEAB), and 40 μL of each sample was transferred into a new tube for labeling. Then, 41 μL of the TMT 10-Plex labeling reagent (90113CH, Thermo Fisher Scientific, USA) was added to each sample and mixed. The tubes were incubated at room temperature for 1 h. Finally, 8 μL of 5% hydroxylamine was added to each sample and incubated for 15 min to terminate the reaction. The labeled peptide solutions were lyophilized and stored at -80 °C.

HPLC analysis

Separation was performed on an Agilent 1100 HPLC System using an Agilent ZORBAX Extend-C18 column (5 μm, 150 mm × 2.1 mm). Mobile phases A (2% acetonitrile [ACN] in HPLC-grade water) and B (90% ACN in HPLC-grade water) were used for the gradient. The solvent gradient was as follows: 0–8 min, 98% A; 8–8.01 min, 98%-95% A; 8.01–48 min, 95%-75% A; 48–60 min, 75 – 60% A; 60–60.01 min; 60 – 10% A; 60.01–70 min, 10% A; 70–70.01 min, 10–98% A; 70.01–75 min, 98% A. Tryptic peptides were separated at an influent flow rate of 300 μL/min and monitored at 210 nm. Samples were collected over 8–60 min, and the eluents were collected in centrifuge tubes that were marked 1–15 and replaced at one-minute intervals. Samples were recycled in this order until the end of the gradient. The separated peptides were lyophilized for MS.

LC-MS/MS analysis

All analyses were performed with a Q-Exactive HF mass spectrometer (Thermo Fisher Scientific, USA) equipped with a Nanospray Flex ion source (Thermo Fisher Scientific, USA). Samples were applied and separated on a

C18 column (25 cm × 75 μm) in an EASY-nLCTM 1200 system (Thermo Fisher Scientific, USA). The flow rate was set at 300 nL/min, and the total run time was 75 min (0–40 min, 5–28% B; 40–60 min, 28–42% B; 60–65 min, 42–90% B; 65–75 min, 90% B; mobile phase A = 0.1% FA in water and mobile phase B = 0.1% FA in ACN). Full MS scans were acquired over a mass range of 350–1500 m/z with a mass resolution of 60,000, and the automatic gain control (AGC) target value was set at 3×10^6. The Top 20 most intense peaks in the MS spectra were fragmented by higher-energy collisional dissociation (HCD) with a collision energy of 32. MS/MS spectra were obtained at a resolution of 45,000 with an AGC target of 2×10^5 and a maximum injection time of 80 ms. The Q Exactive HF dynamic exclusion was set to 30.0 s, and MS was performed in positive ion mode.

Database search and statistical analyses

Proteome Discoverer (Version 2.4) was used to search the whole raw data thoroughly against the sample protein database. The database search was performed with trypsin digestion specificity and alkylation on cysteine was considered a fixed modification. TMT labeling method was selected for the protein quantification. The global false discovery rate (FDR) was set to 0.01. DEPs were identified using a threshold fold change of ≥ 2 and a P value of < 0.05. Annotation of all identified proteins was performed using GO terms (http://www.blast2go.com/b2ghome; http://geneontology.org/) and KEGG pathways (http://www.genome.jp/kegg/). DEPs were further subjected to GO and KEGG enrichment analyses.

Statistical analysis

For the mouse experiment, each group was assigned a sample size of $n \geq 5$. All power values in the mouse studies exceeded 0.8.

For human studies, preliminary data revealed that the differences in plasma GP73 levels among healthy individuals, CRNLM, and CRLM exceeded 150%, with a standard error of the mean (SEM) within groups of ≤ 20%. To achieve a power (1-β) of 0.8 with a significance level (α) of 0.05 and an effect size of ≥ 1.4, a minimum sample size of ≥ 10 subjects per group was calculated.

The data are presented as the means ± SEMs or medians (interquartile ranges). Two-tailed Student's t test was used to evaluate differences between two independent samples, while one-way or two-way ANOVA with the Bonferroni correction was employed to analyze differences among multiple samples. Differences in categorical variables among the three groups were analyzed using the chi-square test. The significance levels were determined as follows: n. s. (not significant), $P > 0.05$; *, $P < 0.05$; **, $P < 0.01$; and ***, $P < 0.001$. Statistical analyses were conducted using GraphPad Prism 8.0.

Supplementary Information

The online version contains supplementary material available at https://doi.org/10.1186/s12943-025-02350-6.

Supplementary Material 1

Author contributions

L. Huang: Conceptualization, data curation, software, formal analysis, validation, investigation, visualization, methodology, writing-original draft, writing-review and editing. M. Wei: Conceptualization, data curation, formal analysis, validation, visualization, methodology, writing-original draft. H. Li: Data curation, formal analysis, writing-review and editing. M. Yu: Data curation, formal analysis, writing-review and editing. L. Wan: Conceptualization, funding acquisition, data curation, software, formal analysis, investigation, visualization, methodology. R. Zhao: Conceptualization, data curation, software, formal analysis, investigation, visualization, methodology. Q. Gao: Conceptualization, resources, data curation, formal analysis, writing-review and editing. L. Sun: Data curation, software, formal analysis, investigation, visualization, methodology. X. Hou: Data curation, software, formal analysis, investigation, visualization, methodology. Y. Mo: Data curation, formal analysis, visualization. Q. Huang: Data curation, formal analysis, visualization. L. Zhen: Data curation, formal analysis, visualization. X. Yang: Data curation, formal analysis, visualization. J. Li: Data curation, formal analysis, visualization. N. Wang: Conceptualization, resources, formal analysis, visualization. C. Zhang: Conceptualization, resources, formal analysis, visualization. H. Jin: Conceptualization, resources, formal analysis, visualization. L. Zhou: Data curation, formal analysis, visualization. Y. Xu: Data curation, formal analysis, visualization. H. Lin: Data curation, formal analysis, visualization. X. Zhang: Data curation, formal analysis, visualization. B. Li: Conceptualization, resources, supervision, writing-review and editing. Y. Han: Conceptualization, resources, supervision, writing-review and editing. J. Yuan: Conceptualization, resources, supervision, funding acquisition, writing-review and editing. R. Zhang: Conceptualization, resources, supervision, project administration, writing-review and editing. F. Wu: Conceptualization, resources, supervision, funding acquisition, project administration, writing-original draft and writing-review and editing. H. Zhong: Conceptualization, resources, supervision, funding acquisition, writing-original draft and writing-review and editing. C. Wei: Conceptualization, resources, supervision, funding acquisition, project administration, writing-original draft and writing-review and editing.

Funding

This work was funded by grants from Beijing Nova Program (20240484702), National Natural Science Foundation of China (32070755, 32100558, 32270823, 81773205, 82070595, and 82360537), Youth Fund Project of Guangxi Medical University Cancer Hospital (2024-02), Key Laboratory of High-Incidence-Tumor Prevention and Treatment, Ministry of Education, China (GKE-ZZ202004 and GKE-ZZ202129), and Key Laboratory of Early Prevention and Treatment for Regional High Frequency Tumor, Ministry of Education, China (GKE-ZZ202216 and GKE-ZZ202309).

Data availability

Data supporting the findings of this study are available within the article and its supplementary materials. The MS proteomics data have been deposited to the ProteomeXchange Consortium via the iProX partner repository with the data set identifier PXD042963.

Declarations

Ethics approval and consent to participate

The use of patient samples in this study was approved by the Ethics Committee of Guangxi Medical University Cancer Hospital (LW2023060). All animal experiments were conducted at the AMMS Animal Center (Beijing, China) and were reviewed and approved by the Institutional Animal Care and Use Committee (IACUC-DWZX-2023-022).

Consent for publication

All authors read and approved the final manuscript.

Notes
No author disclosures were reported.

Competing interests
The authors declare no competing interests.

Author details
[1]Laboratory of Advanced Biotechnology, Beijing Institute of Biotechnology, No. 20 Dongdajie, Fengtai District, Beijing 100071, China
[2]Hepatobiliary Surgery Department, Guangxi Medical University Cancer Hospital, No. 71 Hedi Road, Qingxiu District, Nanning, Guangxi 530021, China
[3]Key Laboratory of Early Prevention and Treatment for Regional High Frequency Tumor, Guangxi Medical University, Ministry of Education, Nanning, Guangxi 530021, China
[4]Department of Gastroenterology, Beijing Friendship Hospital, Capital Medical University, National Clinical Research Center for Digestive Disease, State Key Laboratory of Digestive Health, Beijing Key Laboratory of Early Gastrointestinal Cancer Medicine and Medical Devices, No. 95 Yong'an Road, Xicheng District, Beijing 100050, China
[5]Beijing Youngen Technology Co. Ltd, No. 55 Qingfeng West Road, Daxing District, Beijing 102629, China
[6]Department of Radiotherapy, Changzhi People's Hospital, No. 502, Changxing Middle Road, Luzhou District, Changzhi, Shanxi 046000, China
[7]Department of Surgical Oncology and Central Laboratory, the Fourth Affiliated Hospital of China Medical University, No. 4, Chongshan East Road, Huanggu District, Shenyang, Liaoning 110032, China
[8]Department of Colorectal Surgery, Liaoning Cancer Hospital and Institute, Cancer Hospital of Dalian University of Technology, No. 44 Xiaoheyan Road, Dadong Distrct, Shenyang, Liaoning 110042, China
[9]Clinical Laboratory, the Fifth Medical Center of Chinese People's Liberation Army General Hospital, No. 100 Xisihuan Middle Road, Beijing 100039, China
[10]Department of Interventional Therapy, National Cancer Center/National Clinical Research Center for Cancer/Cancer Hospital, Chinese Academy of Medical Sciences and Peking Union Medical College, No. 17 Panjiayuan South Road, Chaoyang District, Beijing 100021, China
[11]Capital Institute of Pediatrics, Capital Center for Children's Health, Capital Medical University, No. 2 Yabao Road, Chaoyang District, Beijing 100020, China

Received: 3 January 2025 / Accepted: 9 May 2025
Published online: 26 May 2025

References

1. Xi Y, Xu P. Global colorectal cancer burden in 2020 and projections to 2040. Transl Oncol. 2021;14:101174. https://doi.org/10.1016/j.tranon.2021.101174.
2. Rawla P, Sunkara T, Barsouk A. Epidemiology of colorectal cancer: incidence, mortality, survival, and risk factors. Prz Gastroenterol. 2019;14:89–103. https://doi.org/10.5114/pg.2018.81072.
3. Hossain MS, et al. Colorectal cancer: A review of carcinogenesis, global epidemiology, current challenges, risk factors, preventive and treatment strategies. Cancers (Basel). 2022;14. https://doi.org/10.3390/cancers14071732.
4. Aziz H, Ahmed Z, Lee Y, Drumm G, Saif MW. A comprehensive review of management of colorectal liver Mets in the current era. Cancer Med J. 2022;5:46–57.
5. Zhou H, et al. Colorectal liver metastasis: molecular mechanism and interventional therapy. Signal Transduct Target Ther. 2022;7:70. https://doi.org/10.1038/s41392-022-00922-2.
6. Manfredi S, et al. Epidemiology and management of liver metastases from colorectal cancer. Ann Surg. 2006;244:254–9. https://doi.org/10.1097/01.sla.0000217629.94941.cf.
7. Wang J, et al. Metastatic patterns and survival outcomes in patients with stage IV colon cancer: A population-based analysis. Cancer Med. 2020;9:361–73. https://doi.org/10.1002/cam4.2673.
8. Nordlinger B, et al. Combination of surgery and chemotherapy and the role of targeted agents in the treatment of patients with colorectal liver metastases: recommendations from an expert panel. Ann Oncol. 2009;20:985–92. https://doi.org/10.1093/annonc/mdn735.
9. Helling TS, Martin M. Cause of death from liver metastases in colorectal cancer. Ann Surg Oncol. 2014;21:501–6. https://doi.org/10.1245/s10434-013-3297-7.
10. Konopke R, et al. Colorectal liver metastases: an update on palliative treatment options. J Gastrointestin Liver Dis. 2012;21:83–91.
11. Bu P, et al. Aldolase B-Mediated Fructose metabolism drives metabolic reprogramming of Colon cancer liver metastasis. Cell Metab. 2018;27:1249–62. https://doi.org/10.1016/j.cmet.2018.04.003. e1244.
12. Ragusa S, et al. PROX1 promotes metabolic adaptation and fuels outgrowth of Wnt(high) metastatic colon cancer cells. Cell Rep. 2014;8:1957–73. https://doi.org/10.1016/j.celrep.2014.08.041.
13. Lv Y, Zhang HJ. Effect of Non-alcoholic fatty liver disease on the risk of synchronous liver metastasis: analysis of 451 consecutive patients of newly diagnosed colorectal Cancer. Front Oncol. 2020;10:251. https://doi.org/10.3389/fonc.2020.00251.
14. Wang Z, et al. Extracellular vesicles in fatty liver promote a metastatic tumor microenvironment. Cell Metab. 2023. https://doi.org/10.1016/j.cmet.2023.04.013.
15. Annett S, Moore G, Robson T. Obesity and Cancer metastasis: molecular and translational perspectives. Cancers (Basel). 2020;12. https://doi.org/10.3390/cancers12123798.
16. Li Y, et al. Hepatic lipids promote liver metastasis. JCI Insight. 2020;5. https://doi.org/10.1172/jci.insight.136215.
17. Chan WK. Comparison between obese and non-obese nonalcoholic fatty liver disease. Clin Mol Hepatol. 2023;29:S58–67. https://doi.org/10.3350/cmh.2022.0350.
18. DiStefano JK, Gerhard GS. NAFLD in normal weight individuals. Diabetol Metab Syndr. 2022;14:45. https://doi.org/10.1186/s13098-022-00814-z.
19. Golabi P, et al. Patients with lean nonalcoholic fatty liver disease are metabolically abnormal and have a higher risk for mortality. Clin Diabetes. 2019;37:65–72. https://doi.org/10.2337/cd18-0026.
20. Di Bella MA, Overview, Update on Extracellular Vesicles. Considerations on exosomes and their application in modern medicine. Biology (Basel). 2022;11. https://doi.org/10.3390/biology11060804.
21. Zhang Y, Liu Y, Liu H, Tang WH. Exosomes: biogenesis, biologic function and clinical potential. Cell Biosci. 2019;9:19. https://doi.org/10.1186/s13578-019-0282-2.
22. Albacete-Albacete L, et al. ECM deposition is driven by caveolin-1-dependent regulation of Exosomal biogenesis and cargo sorting. J Cell Biol. 2020;219. https://doi.org/10.1083/jcb.202006178.
23. Hessvik NP, Llorente A. Current knowledge on exosome biogenesis and release. Cell Mol Life Sci. 2018;75:193–208. https://doi.org/10.1007/s00018-017-2595-9.
24. Whiteside TL. Tumor-Derived exosomes and their role in Cancer progression. Adv Clin Chem. 2016;74:103–41. https://doi.org/10.1016/bs.acc.2015.12.005.
25. Titu S, et al. Exosomes in colorectal cancer: from physiology to clinical applications. Int J Mol Sci. 2023;24. https://doi.org/10.3390/ijms24054382.
26. Kalluri R, LeBleu VS. The biology, function, and biomedical applications of exosomes. Science. 2020;367. https://doi.org/10.1126/science.aau6977.
27. Bai S, et al. Tumor-Derived exosomes modulate primary site tumor metastasis. Front Cell Dev Biol. 2022;10:752818. https://doi.org/10.3389/fcell.2022.752818.
28. Yang X, et al. The key role of exosomes on the Pre-metastatic niche formation in tumors. Front Mol Biosci. 2021;8:703640. https://doi.org/10.3389/fmolb.2021.703640.
29. Hu L, Li L, Xie H, Gu Y, Peng T. The golgi localization of GOLPH2 (GP73/GOLM1) is determined by the transmembrane and cytoplamic sequences. PLoS ONE. 2011;6:e28207. https://doi.org/10.1371/journal.pone.0028207.
30. Liu Y, et al. Golgi phosphoprotein 73: the driver of Epithelial-Mesenchymal transition in Cancer. Front Oncol. 2021;11:783860. https://doi.org/10.3389/fonc.2021.783860.
31. Xia Y, et al. Golgi protein 73 and its diagnostic value in liver diseases. Cell Prolif. 2019;52:e12538. https://doi.org/10.1111/cpr.12538.
32. Wang Y, Wan YY. Golgi protein 73, hepatocellular carcinoma and other types of cancers. Liver Res. 2020;4:161–7. https://doi.org/10.1016/j.livres.2020.09.003.
33. Peng Y, et al. GP73 is a TBC-domain Rab GTPase-activating protein contributing to the pathogenesis of non-alcoholic fatty liver disease without obesity. Nat Commun. 2021;12:7004. https://doi.org/10.1038/s41467-021-27309-1.
34. Wan L, et al. GP73 is a glucogenic hormone contributing to SARS-CoV-2-induced hyperglycemia. Nat Metab. 2022;4:29–43. https://doi.org/10.1038/s42255-021-00508-2.

35. Yang X, et al. GP73 Blockade alleviates abnormal glucose homeostasis in diabetic mice. J Mol Endocrinol. 2023;70. https://doi.org/10.1530/JME-22-0103.
36. Zhang J, et al. A meta-analysis of the prognostic significance of golgi protein 73 in hepatocellular carcinoma in Chinese patients. Arch Med Sci. 2020;16:1104–10. https://doi.org/10.5114/aoms.2019.83821.
37. Jiao C, Cui L, Piao J, Qi Y, Yu Z. Clinical significance and expression of serum golgi protein 73 in primary hepatocellular carcinoma. J Cancer Res Ther. 2018;14:1239–44. https://doi.org/10.4103/0973-1482.199784.
38. Han QF, et al. Exosome biogenesis: machinery, regulation, and therapeutic implications in cancer. Mol Cancer. 2022;21:207. https://doi.org/10.1186/s12943-022-01671-0.
39. Shearer LJ, Petersen NO. Distribution and Co-localization of endosome markers in cells. Heliyon 5, e02375 (2019). https://doi.org/10.1016/j.heliyon.2019.e02375
40. Gal Z, et al. Mutations of the central tyrosines of putative cholesterol recognition amino acid consensus (CRAC) sequences modify folding, activity, and sterol-sensing of the human ABCG2 multidrug transporter. Biochim Biophys Acta. 2015;1848:477–87. https://doi.org/10.1016/j.bbamem.2014.11.006.
41. Liang J, et al. The effect of PPP2CA expression on the prognosis of patients with hepatocellular carcinoma and its molecular biological characteristics. J Gastrointest Oncol. 2021;12:3008–21. https://doi.org/10.21037/jgo-21-720.
42. Lai M-W, Liang K-H, Yeh C-T, Hepatitis B. Virus PreS/S Truncation mutant rtM204I/sW196* increases carcinogenesis through deregulated HIF1A, MGST2, and TGFbi. Int J Mol Sci. 2020;21:6366–78.
43. Tan F, et al. Neuron navigator 2 overexpression indicates poor prognosis of colorectal cancer and promotes invasion through the SSH1L/cofilin-1 pathway. J Exp Clin Cancer Res. 2015;34:117. https://doi.org/10.1186/s13046-015-0237-3.
44. Krause N, Wegner A. Fructose metabolism in Cancer. Cells. 2020;9. https://doi.org/10.3390/cells9122635.
45. Bojkova B, Winklewski PJ, Wszedybyl-Winklewska M. Dietary fat and Cancer-Which is good, which is bad, and the body of evidence. Int J Mol Sci. 2020;21. https://doi.org/10.3390/ijms21114114.
46. Kladney RD, Cui X, Bulla GA, Brunt EM, Fimmel CJ. Expression of GP73, a resident golgi membrane protein, in viral and nonviral liver disease. Hepatology. 2002;35:1431–40. https://doi.org/10.1053/jhep.2002.32525.
47. Liang YJ, Duan L, Lu JP, Xia J. Engineering exosomes for targeted drug delivery. Theranostics. 2021;11:3183–95. https://doi.org/10.7150/thno.52570.
48. Zhong Y, et al. Exosomes: A new pathway for Cancer drug resistance. Front Oncol. 2021;11:743556. https://doi.org/10.3389/fonc.2021.743556.
49. Ludwig N, et al. Isolation and analysis of Tumor-Derived exosomes. Curr Protoc Immunol. 2019;127:e91. https://doi.org/10.1002/cpim.91.
50. Hu W, et al. NAV2 facilitates invasion of cutaneous melanoma cells by targeting SNAI2 through the GSK-3beta/beta-catenin pathway. Arch Dermatol Res. 2019;311:399–410. https://doi.org/10.1007/s00403-019-01909-w.
51. M., P. et al. Molecular features and gene expression signature of metastatic colorectal cancer. Oncol Rep 45, 10 (2021).
52. P., H., L., L., S., X. & X., W. Exosomes derived from colon cancer cells and plasma of colon cancer patients promote migration of SW48 cells through Akt/mTOR pathway. Pathol Res Pract 222, 153454 (2021).
53. F. S. S O., M. F. Exosomes from metastatic cancer cells transfer amoeboid phenotype to non-metastatic cells and increase endothelial permeability: their emerging role in tumor heterogeneity. Sci Rep. 2017;7:4711.
54. Sun B, Karin M. Obesity, inflammation, and liver cancer. J Hepatol. 2012;56:704–13. https://doi.org/10.1016/j.jhep.2011.09.020.
55. Fujiwara-Tani R, et al. Diabetes mellitus is associated with liver metastasis of colorectal cancer through production of biglycan-rich cancer stroma. Oncotarget. 2020;11:2982–94. https://doi.org/10.18632/oncotarget.27674.
56. Wu Q, Zhou L, Lv D, Zhu X, Tang H. Exosome-mediated communication in the tumor microenvironment contributes to hepatocellular carcinoma development and progression. J Hematol Oncol. 2019;12:53. https://doi.org/10.1186/s13045-019-0739-0.
57. Liu J, et al. The role of the golgi apparatus in disease (Review). Int J Mol Med. 2021;47. https://doi.org/10.3892/ijmm.2021.4871.
58. Sengupta P, et al. ER trapping reveals golgi enzymes continually revisit the ER through a recycling pathway that controls golgi organization. Proc Natl Acad Sci U S A. 2015;112:E6752–6761. https://doi.org/10.1073/pnas.1520957112.
59. daSilva LL, et al. Endoplasmic reticulum export sites and golgi bodies behave as single mobile secretory units in plant cells. Plant Cell. 2004;16:1753–71. https://doi.org/10.1105/tpc.022673.
60. Huang L, et al. Role of lipid rafts in Porcine reproductive and respiratory syndrome virus infection in MARC-145 cells. Biochem Biophys Res Commun. 2011;414:545–50.

Publisher's note